

Synthetic Data for Robust Stroke Segmentation

Liam Chalcraft ¹ , Ioannis Pappas ² , Cathy J. Price ¹ , John Ashburner ¹ 

¹ Wellcome Centre for Human Neuroimaging, University College London

² University of Southern California

Abstract

Current deep learning-based approaches to lesion segmentation in neuroimaging often depend on high-resolution images and extensive annotated data, limiting clinical applicability. This paper introduces a novel synthetic data framework tailored for stroke lesion segmentation, expanding the SynthSeg methodology to incorporate lesion-specific augmentations that simulate diverse pathological features. Using a modified nnUNet architecture, our approach trains models with label maps from healthy and stroke datasets, facilitating segmentation across both normal and pathological tissue without reliance on specific sequence-based training. Evaluation across in-domain and out-of-domain (OOD) datasets reveals that our method matches state-of-the-art performance within the training domain and significantly outperforms existing methods on OOD data. By minimizing dependence on large annotated datasets and allowing for cross-sequence applicability, our framework holds potential to improve clinical neuroimaging workflows, particularly in stroke pathology. PyTorch training code and weights are publicly available at <https://github.com/liamchalcraft/SynthStroke>, along with an SPM toolbox featuring a plug-and-play model at <https://github.com/liamchalcraft/SynthStrokeSPM>.

Keywords

Machine Learning, Image Segmentation, Domain Adaptation

Article informations

©2024 Chalcraft, Pappas, Price and Ashburner. License: CC-BY 4.0

1. Introduction

Dense classification of images or volumes, known as semantic segmentation, is crucial in many neuroimaging and medical imaging analysis pipelines. Properties such as volume and surface distance of healthy tissue structures are used in longitudinal models to measure anatomical changes, while tumor labels are essential for radiotherapy planning. Extracting fine-grained labels has typically been limited to high-contrast, high-resolution structural scans, such as those acquired using the MPRAGE sequence, which are rarely found in clinical settings. This limitation poses a significant barrier to applying these methods in clinical practice.

Both traditional probabilistic methods (Ashburner and Friston, 2005) and modern deep discriminative methods (Isensee et al., 2020) require prior information to be provided for a given sequence - in the case of a traditional method this may be an atlas or template, and in modern methods this would come in the form of training data. Atlas-based methods build a template of the anatomical structure of the brain, which may be deformed into alignment with a new subject to assign voxel-wise anatomical classes. This is proven to be robust for delineating healthy structure even with shifts in contrast (Puonti et al., 2016), however it is non-trivial to include classes of pathology such

as stroke within such a model, due to the inherent heterogeneity in location and geometric properties. In the context of generative models, lesions may be included in the form of anomaly detection as demonstrated in Seghier et al. (2008). This method is not however directly attempting to label the pathology, and (by design) will label physiological changes such as ventricular enlargement in addition to the responsible infarct.

Deep discriminative models trained using supervised learning have been able to reach human-level performance when tested in-domain on large datasets for a variety of brain pathologies and imaging modalities (Baid et al., 2021; de la Rosa et al., 2024). There is still however a significant gap when trying to translate these models to clinical data, where each hospital is likely to vary both in the scanning equipment used and the choice of imaging sequences (Nguyen et al., 2024). This poses a significant challenge to the adoption of deep learning for automating the labelling of clinical data, which could greatly help to accelerate the translation of modern research in stroke prognosis (Loughnan et al., 2019).

To extend such methods to the open-ended domain of clinical scans, models often need to perform on sequences for which no training data may be available. To this end, domain randomisation via synthetic data has been shown

to give impressive results for healthy brain parcellation in SynthSeg (Billot et al., 2023). In this method, a set of ground truth healthy tissues are used to generate synthetic images, under the assumption that each tissue class’ intensity distribution should roughly follow a Gaussian. By assigning random Gaussian distributions to each class, a deep learning model can learn to extract shape information for parcellation in a way that is invariant to the input image’s relative tissue contrast, hence allowing the model to be used on any sequence at test-time, without training data or prior knowledge of the sequence. This method of training with synthetic data has since been extended to tasks such as image registration (Hoffmann et al., 2022, 2023, 2024), image super-resolution (Iglesias et al., 2021, 2023), surface estimation (Gopinath et al., 2023, 2024a) and vascular segmentation (Chollet et al., 2024). A comprehensive overview is available in Gopinath et al. (2024b).

An additional benefit of this method is that the ‘forward model’ of creating an MRI (or CT) image from tissues of different physical properties is a perfect 1:1 mapping to the ‘inverse model’ of labeling the tissues (i.e. segmentation) from the acquired image. In structures that exhibit a large amount of inter-rater variability, this is likely to help prevent a model from imitating under- or over- segmentation from imperfect ground truths - the images segmented are generated from the corresponding segmentation labels and so labels will always be a consistent method of segmentation.

Prior work to SynthSeg demonstrated the potential of encoding anatomical priors in a neural network through pre-training with unpaired parcellation labels (Dalca et al., 2018). Such methods face significantly larger challenges when applied to the heterogeneous shape and spatial distribution of lesions. In healthy parcellation, anatomical structures have consistent positions across individuals (e.g., the brainstem reliably appears in the same region of the brain), a regularity that has motivated atlas-based approaches to parcellation. In contrast, lesions are highly variable across individuals—not only in number and size but also in their spatial distribution. Unlike anatomical structures, lesions cannot be reliably mapped to a specific location or shape within an atlas. Although the exact site of lesion initiation is often influenced by the brain’s vascular architecture—meaning that certain regions are statistically more susceptible to stroke due to the location of large blood vessels—the resulting lesion’s size, shape, and spread are highly variable. Multiple sclerosis serves as an exception, with lesions that are somewhat predictable in their white matter localisation (Lassmann, 2018), enabling modelling through synthetic deep learning frameworks (Billot et al., 2021) and traditional probabilistic models (Cerri et al., 2021). More recently, Liu et al. (2024) has shown promising results by training a SynthSeg-like model on lesion la-

bels from various pathologies, providing a foundation for fine-tuning on multiple downstream datasets. However, achieving a model that can seamlessly generalise for open-domain stroke segmentation remains an active area of research

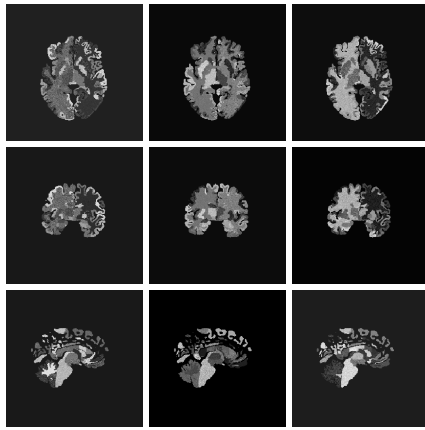
In our work, we extend the SynthSeg framework to the task of stroke lesion segmentation via a novel lesion-pasting method that better simulates variety in lesion appearance. We show that this can be used to expand an existing segmentation dataset to attain competitive performance in-domain, and state-of-the-art performance out-of-domain that can be further enhanced with existing test-time domain adaptation techniques. We validate this on a comprehensive range of lesion datasets with a wide distribution of image characteristics and lesion physiology. To assist in widespread evaluation of this framework, we release PyTorch training code/weights, and a MATLAB toolbox for SPM to reduce the barrier to clinical adoption.

2. Methods

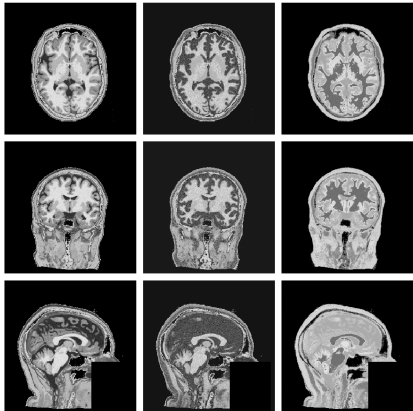
The core premise of our training procedure is to generate synthetic images with paired labels by combining random permutations of healthy tissue labels and binary stroke lesion maps.

A number of important modifications were made from the original SynthSeg procedure to better suit it to the task of stroke segmentation. First, as we are ultimately only interested in annotating stroke infarct and not the surrounding anatomy, we can opt for a much simpler set of labels than the full set of anatomical labels generated from Freesurfer in SynthSeg. For our experiments we opt for the posterior maps generated using the MultiBrain toolbox in SPM (Brudfors et al., 2020). This reduces the number of sampled healthy labels to only 9 classes, and requires using a single model to generate labels instead of the two used in SynthSeg. A comparison of the sampled labels from Freesurfer and MultiBrain can be seen in Figure 1. Sampled labels are summed using a weighting based on their posterior likelihoods, allowing for the simulation of partial volume. Of these classes, only 4 are labels of brain tissue (Gray Matter (GM), White Matter (WM), GM/WM partial volume and Cerebrospinal Fluid (CSF)) which also makes for a lower memory footprint in training. In all Synth-model training, we opt for predicting these 4 tissue classes in addition to the lesion class in order to prevent issues of class imbalance that can occur when treating lesion segmentation as a binary task.

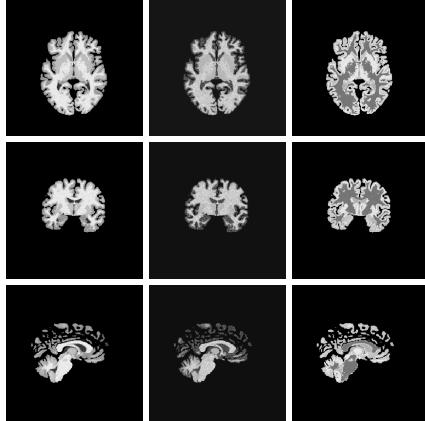
We also enhance the default training procedure by introducing lesion-specific augmentations to mimic variability in lesion appearance. We first use the Soft-CP algorithm (Dai et al., 2022) with random dilations and erosions to vary how the infarct is blended into its neighbouring healthy



(a) Freesurfer (Puonti et al., 2016)



(b) MultiBrain (Brudfors et al., 2020)



(c) MultiBrain (skull-stripped)

Figure 1: Sample generated images using different labels for a single subject. 1a: Freesurfer anatomical labels. 1b: MultiBrain tissue labels. 1c: MultiBrain tissue labels masked to simulate skull-stripping.

tissue. We also introduce a spatially varying multiplicative field to the binary lesion map, which mimics the variety in the local texture of a lesion and presence of penumbra within a stroke. This is performed by applying the MONAI Random Bias Field augmentation (Cardoso et al., 2022) and thresholding the result in the $[0, 1]$ range. A similar approach was adopted in Middleton et al. (2024) and

showed in improvement in model sensitivity.

A model was trained using a combination of healthy labels from the OASIS-3 dataset (LaMontagne et al., 2019) and lesion masks from the ATLAS dataset (Liew et al., 2022). In the OASIS-3 dataset ($N=2679$, 2579:100 train-val split), tissue labels were extracted using SPM’s MultiBrain (Brudfors et al., 2020) and spatially aligned to ICBM space to enable correct lesion placement. The ATLAS dataset ($N=655$, 419:105:131 train-val-test split) was used for pasting lesion maps, which were also aligned to ICBM space. A lesioned brain map was generated by randomly pasting an ATLAS lesion label onto an OASIS subject’s parcellation using the previously described augmentations.

The generated maps were used to randomly assign Gaussians to each tissue class by sampling a mean from the distribution $\mu \sim \text{Uniform}(0, 255)$, a standard deviation $\sigma \sim \text{Uniform}(0, 16)$ and the FWHM of the applied smoothing from $\text{Uniform}(0, 2)$. All images were then extensively augmented using a variety of transformations. These include the application of a random bias field, which involves rescaling intensities based on a smooth multiplicative field controlled by a number of control points $\mathcal{U}(2, 7)$ and a bias strength $\mathcal{U}(0, 0.5)$, with multiplicative values sampled from $\mathcal{U}(1 - \text{strength}, 1 + \text{strength})$. Random affine deformation is also employed, consisting of random rotations within $\mathcal{U}(-15, 15)$ degrees, shearing within $\mathcal{U}(0, 0.012)$, and zooming within $\mathcal{U}(0.85, 1.15)$. Additionally, random elastic deformations are applied with a maximum displacement $\mathcal{U}(0, 0.05)$ using control points $\mathcal{U}(0, 10)$. Another transformation simulates random skull-stripping by generating a perfect foreground mask of brain tissues and introducing flaws through random dilation (probability of 0.3, radius of 2) and erosion (probability of 0.3, radius of 4). Random flips are applied across each axis with a probability of 0.8. Random Gaussian noise is introduced, controlled by a signal-to-noise ratio (SNR) $\mathcal{U}(0, 10)$, and smoothed by a g-factor field with smoothness $\mathcal{U}(2, 5)$. Slice anisotropy is simulated by rescaling the slice thickness based on a resolution factor $\mathcal{U}(1, 8)$, with experiments assuming an original isotropic resolution of 1mm^3 . Random contrast adjustment is applied using a gamma factor γ sampled from $10^{\mathcal{N}(0, 0.6)}$, while random motion blurring is simulated using a point-spread function with a full width at half maximum (FWHM) $\mathcal{U}(0, 3)$. Intensities were clipped to the 1st and 99th percentiles and images z-normalised to a zero mean and unit standard deviation. Training was performed at an isotropic spacing of 1 mm and volumes randomly cropped to $192 \times 192 \times 192$. A simplified schematic (with image-quality augmentations removed) is shown in Figure 2.

For the synthetic model (labeled **Synth** in all experiments), a combination of real and synthetic data was used for training. Real data was sampled from the ATLAS dataset (using the same training split from which le-

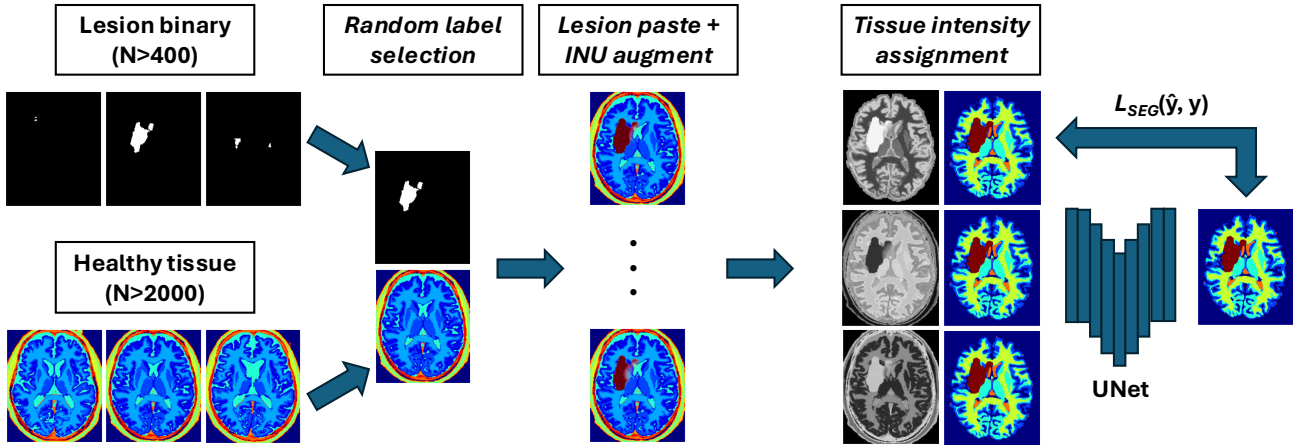


Figure 2: Schematic overview of the data generation process. Lesions are sampled from a template-normalised bank of lesion binary masks, and healthy tissue maps are sampled from a template-normalised bank of MultiBrain segmentations. Pasting of lesions onto healthy tissue maps is performed using a spatially varying lesion intensity to simulate penumbra. Tissue intensities may then be sampled from Gaussian distributions and image-label pairs used to train a segmentation model in a supervised manner.

sion labels were derived). Real MPRAGE images were augmented with random cropping to $192 \times 192 \times 192$, random affine and elastic deformations, histogram normalization, random histogram shift, random field inhomogeneity, random gamma contrast adjustment, and random flipping in all axes, before being z-normalized to zero mean and unit standard deviation. The real and synthetic data loaders were rotated in a weighting based on the number of images present (2579:419 in training for synthetic and real images respectively). In the baseline model (labeled **Baseline** in all experiments), only the real data loader was used with identical transforms, while all other training aspects were kept constant.

A UNet architecture (Ronneberger et al., 2015) was used for this task with the specification used in nnUNet (Isensee et al., 2020) including 6 encoder/decoder stages with output channels (16, 32, 64, 128, 320, 320), with changes to use PReLU activation (He et al., 2015) and one residual unit per block (Isensee et al., 2024). Six output channels were predicted from the network, covering background, the four healthy MultiBrain tissues (gray matter (GM), white matter (WM), gray/white matter partial volume (PV), cerebrospinal fluid (CSF)) and the stroke lesion class. In the baseline model, only the background and stroke lesion classes were predicted. In the case of mixed real/synthetic data, the real images' binary ground truth was treated as a partial ground truth label and loss was only calculated for the stroke lesion class of the prediction. Training was always performed using a single input channel, due to the desire for the model to be generally applicable to any number of available modalities. We propose a naive method for ensembling all available modalities for a subject in Section 3.

Training minimised a combined Dice and Cross Entropy loss. An AdamW optimiser (Loshchilov and Hutter, 2019) was used with a learning rate of 10^{-4} and a decay of 0.01, using a scheduler of $\eta_n = \eta_0(1 - \frac{n}{N})^{0.9}$ for a learning rate η at step $n \in \{1, \dots, N\}$, adapted from nnUNet (Isensee et al., 2020). Gradient clipping was applied for a norm value of 12 to ensure stability (Zhang et al., 2020). A dropout of 0.2 was used during training. Models were trained using a batch size of 1 for 1200 epochs, each of 500 iterations (total 6×10^5 iterations).

2.1 Domain Adaptation

At test-time, we evaluate the utility of a wide range of unsupervised domain adaptation techniques to see if (a) the baseline model could match the Synth model performance with a modern DA method and (b) if the robustness of the Synth model could provide a better starting point for DA to optimise on the new domain. The first of these to be used (referred to in results as '**TTA**') is test-time augmentation (TTA) (Wang et al., 2019). TTA is a popular heuristic for improving robustness of models in out-of-domain (OOD) scenarios and is expected to provide a free improvement on all models' robustness with little risk of corrupting predictions.

The second method to be used (referred to in results as '**DAE**') was the Denoising Autoencoder (DAE) method proposed in Karani et al. (2021): for both the single-label baseline and multi-label Synth model, DAE models were trained to perform cleanup of noise in labels. This method relies on learning to regularise labels to a learned spatial distribution, such that the difference in the before and after of this regularisation can provide an estimate of label degradation. At test-time, a small series of normalisation

layers are prepended to the segmentation model to manipulate the input intensities. This consists of 3 convolution layers with kernel size of 3 and with 16 channels, each followed by a custom activation:

$$f(x) = \exp -\frac{x^2}{\sigma^2}, \quad (1)$$

where the scale factor σ is a learned parameter as described in the original paper. For each image at test-time, this normalisation network is re-initialised and optimised for 100 iterations to minimise the segmentation loss between the segmentation output and the DAE-cleaned output using a combination of Dice and L2 loss. This allows the input image contrast to be manipulated to minimise the difference between the predicted segmentation and the anatomical prior encoded in the DAE. This method relies on using the DAE to encode anatomical priors, and so it is not clear how it will perform given the heterogeneity of stroke lesions.

The next DA method to be used (referred to in results as '**TENT**') is Test-time Entropy Minimisation (TENT) (Wang et al., 2021), where the objective is to maximise model confidence based on the entropy of its predictions. Although the original paper adapts by modifying the batch normalisation statistics, we instead opt to optimise a small normalisation network similar to the DAE workflow due to the limited batch size available when using large 3D volumes. The normalisation network is again re-initialised and optimised for 100 iterations for each test subject, using the Shannon entropy (Shannon, 1948):

$$\mathcal{H}_{\hat{y}} = -\sum p(\hat{y}) \log p(\hat{y}), \quad (2)$$

where $p(\hat{y})$ is the predicted segmentation probability.

The final method to be used is a form of pseudo-labelling (PL), where the entire test dataset is used to optimise all of the segmentation model's parameters. Recent developments in this field focus on ways to clean the predicted pseudo-labels in order to restrict the new supervision to areas of high confidence (Chen et al., 2021). To this end, three forms of PL are evaluated. The first PL method used (referred to in results as '**PL**') simply thresholds the predicted probabilities at a relatively high probability (calculated as $\frac{1.5}{N_C}$ where N_C is the total number of channels including background). In the second PL method (referred to in results as '**UPL**'), the thresholded predictions are further thresholded to include only regions of low uncertainty. Uncertainty is estimated using Monte Carlo dropout (Gal and Ghahramani, 2016) with 10 iterations and thresholded at a value of 0.05 as specified in Chen et al. (2021). The final PL method (referred to in results as '**DPL**') is a reproduction of Chen et al. (2021) and introduces an additional masking based on class prototypes

derived from feature maps in the segmentation model's decoder. In all PL methods, a standard cross-entropy loss is used during optimisation with a class weighting based on the input pseudo-label and models are optimised for 2000 iterations. All DA methods (including DAE and TENT) are optimised using the AdamW optimiser (Loshchilov and Hutter, 2019) with a fixed learning rate of 0.002 and a weight decay of 0.01.

2.2 Pseudo labels

A unique benefit of the proposed Synth framework is its theoretical insensitivity to accuracy of lesion labels. In a standard supervised training framework, we need this label to be a perfect segmentation of the input image. In a synthetic framework, the input images are created *from* the ground truth labels and thus are intrinsically a perfect segmentation. As long as the predictions look like a plausible lesion, then imperfect ground truth labels should be of no detrimental effect in a synthetic framework.

Building on this logic, we explore the benefit of leveraging a large unlabelled dataset via pseudo-labelling. We use the baseline model trained on ATLAS, with TTA for robustness, to infer lesion labels for a private dataset of 1159 isotropic MPRAGE images from the PLORAS study (Seghier et al., 2016) containing chronic stroke.

3. Experiments

Models were validated on a number of datasets. We assessed the models' in-domain performance on the hold-out test set for the **ATLAS** dataset (131 subjects, 1mm isotropic MPRAGE) for in-domain evaluation. For assessing OOD robustness, we use the **ISLES 2015** dataset (Maier et al., 2017) (N=28 subjects, multi-modal MRI), the **ARC** dataset (Gibson et al., 2024; Johnson et al., 2024) (N=229 subjects with T2 images, N=202 with T1, and N=85 with FLAIR) and a private dataset of N=263 subjects with combinations of T2 and FLAIR images resliced to 2mm isotropic and spatially normalised to the MNI template, referred to in this work as **PLORAS** (Price et al., 2010). The ISLES and PLORAS datasets also exhibit an additional domain shift due to the presence of acute pathology instead of chronic. This PLORAS dataset is distinct to the chronic MPRAGE cohort described in Section 2.2.

At test-time, images are loaded, oriented to RAS, resliced to 1 mm slice thickness, histogram normalised and images z-scored to a zero mean and unit standard deviation. Sliding-window inference was performed using a patch size of $192 \times 192 \times 192$, using patches with a 50% overlap and a Gaussian weighting with $\sigma = 0.125$ when combining patches. Test-time augmentation was additionally performed (denoted in results as **TTA**) by averaging logits

across all possible combinations of flips in the x, y and z axes. Predicted logits were then resliced to the original input image and a softmax applied to derive posterior probabilities. An argmax was then used to derive a binary lesion map. TTA is a popular heuristic method for increasing model robustness at test-time (Wang et al., 2019).

Multi-modal ensembling: In addition to per-modality evaluation, we provide results of ensembles of per-modality predictions to better represent how such a model may be used in practice. Logits were averaged first across all modalities before taking the softmax and post-processing as stated previously. Ensemble results are reported for ISLES 2015 and ARC datasets.

Comparison to the ground truth was performed by reslicing both the prediction and ground truth to 1 mm slice thickness and padding images to a size of $256 \times 256 \times 256$. Segmentations were evaluated using the Dice coefficient and 95th-percentile Hausdorff distance (HD95). Further evaluation is reported in Appendix A using absolute volume difference (AVD), absolute lesion difference (ALD), and lesion-wise F1 score (LF1), true positive rate (TPR) and false positive rate (FPR).

The Dice coefficient measures overlap, where a score of 1 indicates perfect overlap and 0 indicates no overlap. The Hausdorff distance measures surface similarity by determining the shortest distance between surfaces at all given points, using the 95th-percentile value to avoid errors from anomalous values in imperfect masks. Note that a prediction of entirely background class will return the maximum side length of 256.

The absolute volume difference (given in units cm^3) gives a direct comparison of the overall proportion of brain labelled as unhealthy. The absolute lesion difference \mathcal{L} is the difference in the number of unique lesions, defined as $\mathcal{L}(x, y) = |\mathcal{C}(x) - \mathcal{C}(y)|$, where \mathcal{C} is an algorithm used to calculate the number of connected components. Lastly, the lesion-wise F1 score uses the same equation as Dice but on a per-lesion basis rather than per-voxel: for each unique lesion in the ground-truth y , if a single voxel of the predicted mask overlaps with the lesion then this is considered as a success. The Sensitivity score is a measure of the detection of true positives, given by $\frac{TP}{TP+FN}$ where TP are true positives and FN are false negatives. The false-positive rate (FPR), the complement of specificity, is given by $1 - \frac{TN}{TN+FP}$ where TN are true negatives and FP are false positives.

Pseudo labels: We generate pseudo labels on the MPRAGE PLORAS dataset using the baseline model with TTA. Predictions are made on images normalised to the MNI template, meaning predictions are aligned to the healthy tissue maps. A new baseline model is then trained using the predicted image-label pairs combined with the original ATLAS training data. Likewise, a new Synth model

is trained where labels are added to the set of label maps used for pasting, whilst the mixed healthy data is restricted to still only include the manually-labelled ATLAS dataset. These models are trained with the exact same settings as used for the original Synth and baseline models.

4. Results

Overall results are shown in Figure 3 for both models and their best-performing domain adaptation technique. Comparisons of all adaptation techniques can be seen in Tables 1, 2, 3 and 4.

4.1 ATLAS

In the ATLAS dataset, the task is considered completely in-domain so the Baseline model was expected to outperform the Synth model due to simulated data not containing all possible biomarkers from real images. As shown in Figure 3, the Baseline model performed as expected but the Synth model remained competitive, losing only in Dice and AVD. Table 1 shows that no differences between the two models are statistically significant. Table 11 shows that the Baseline model reported a greater mean TPR with and without TTA, at the expense of a higher FPR indicating a greater tendency to over-segment. The baseline having a better AVD and worse ALD, suggests that this over-segmentation may be due to mis-identifying lesions rather than over-extending the boundary of correctly identified lesions.

Table 1: Mean results on the ATLAS hold-out set (N=131). Best score shown in bold. Student’s t distribution 95% confidence intervals given in brackets.

Modality	Model	Dice	HD95
T1w	Baseline	0.575 (0.523-0.627)	23.5 (13.9-33.2)
	Baseline+TTA	0.575 (0.522-0.628)	19.7 (10.2-29.3)
	Synth	0.482 (0.431-0.534)	22.6 (12.0-33.3)
	Synth+TTA	0.498 (0.446-0.550)	23.0 (11.6-34.5)

4.2 ISLES 2015

The ISLES 2015 dataset was the first benchmark used to evaluate behavior in OOD settings. The results in Figure 3 and Table 2 show that the Synth model outperforms the Baseline model in all modalities except T1w and DWI in regards to Dice with high statistical significance. It is worth noting that, in modalities where models performed relatively poorly, the FPR scores were higher without a large decrease in TPR (Table 12). This suggests that the poor performance in OOD may be attributable to false positives rather than false negatives. Both models scored lower on this dataset’s T1w data than for the in-domain ATLAS T1w data, possibly due to differences between sub-acute strokes in the dataset and the chronic stroke images

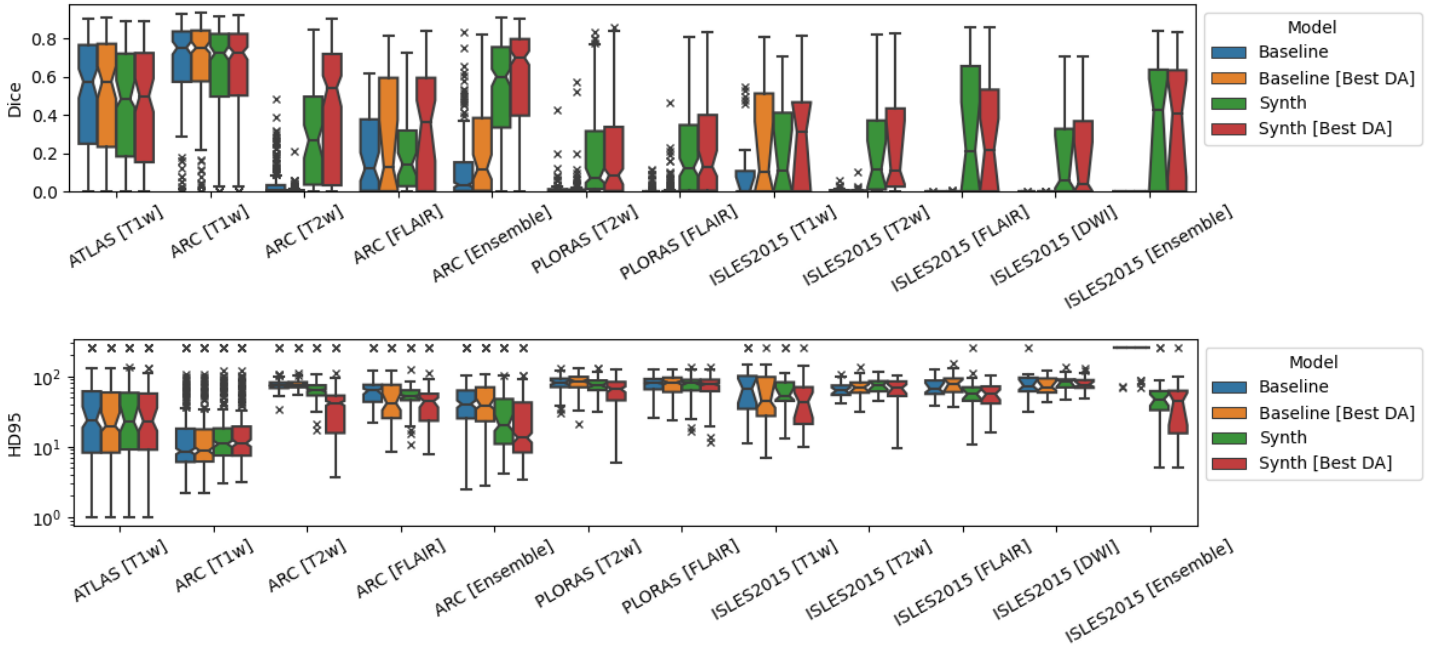


Figure 3: Dice and 95th-percentile Hausdorff Distance for all reported datasets. 'Best DA' indicates the best-performing domain adaptation technique for the model on the given dataset/modality.

used in training.

Table 2 also reports all results for DA methods using both the baseline and Synth models. For the baseline model, in all cases except the near-domain T1w modality the DA methods fail to recover any accuracy from the initial model. In the case of T1w, only the DAE method leads to an improvement in Dice score. For the Synth data, in all modalities there is always at least one DA technique that leads to an improvement in Dice and HD95, with statistically significant improvements over the baseline visible in T1w and Ensemble modalities. This provides evidence that the more robust Synth model may provide an ideal starting point for DA techniques.

In an ensemble of the four modalities available per-subject, for all instances the Baseline model failed and gave an empty prediction leading to the zero Dice scores observed in Table 2. In contrast, the Synth model's ensemble prediction significantly outperformed any of the single modalities in Dice score. A visualisation of the ensemble predictions can be seen in Figure 4. It is also noted that ensembling is expected to reduce the likelihood of models mis-labelling irrelevant hyperintensity in sequences such as FLAIR and DWI.

4.3 ARC

The ARC dataset is a dataset of research-quality scans for chronic stroke patients, and should therefore represent a less dramatic domain shift. The T1w results in Table 3, which represent the closest domain to training, support this expectation with both the baseline and the Synth model

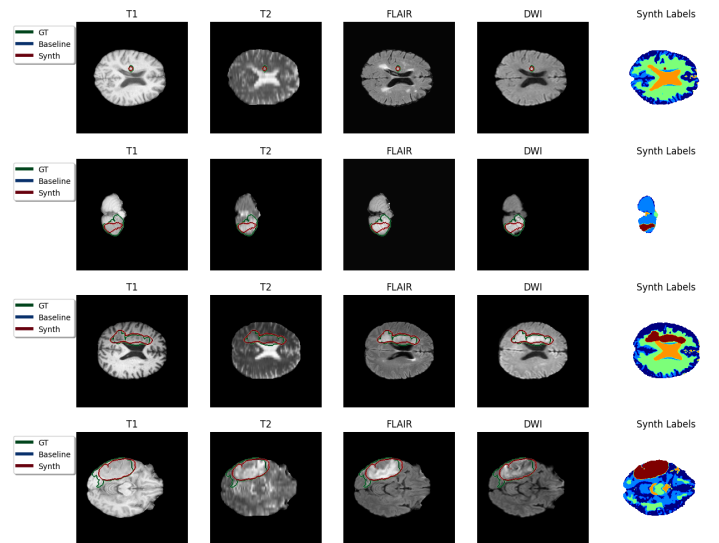


Figure 4: Sample TTA predictions with ensembling method in the ISLES 2015 dataset. Color code in predicted Synth labels: dark-blue = Gray Matter, green = White Matter, light-blue = Gray/White Matter partial volume, amber = CSF, red = stroke.

achieving strong Dice and HD95 scores with no statistical significance between them. The results for the T2 modality and the overall ensemble support the Synth model's performance in OOD scenarios, demonstrating a statistically significant improvement over the baseline. The T1w performance in both models is significantly higher in Dice than the Synth model's ensemble result, however there is no significant difference in HD95. The ensemble scenario

Table 2: Median results on the ISLES2015 dataset (N=28). Best score shown in bold. Student’s t distribution 95% confidence intervals given in brackets.

Modality	Model	Dice	HD95
T1w	Baseline	0.000 (0.000-0.074)	67.0 (39.7-94.2)
	Baseline+TTA	0.000 (0.000-0.064)	69.8 (30.0-109.7)
	Baseline+TENT	0.000 (0.000-0.004)	256.0 (216.6-295.4)
	Baseline+DAE	0.105 (0.000-0.217)	44.1 (22.1-66.2)
	Baseline+PL	0.006 (0.000-0.028)	76.8 (70.5-83.2)
	Baseline+UPL	0.000 (0.000-0.000)	256.0 (256.0-256.0)
	Baseline+DPL	0.000 (0.000-0.000)	256.0 (256.0-256.0)
	Synth	0.110 (0.012-0.208)	52.5 (29.9-75.0)
	Synth+TTA	0.088 (0.000-0.188)	44.8 (11.1-78.4)
	Synth+TENT	0.000 (0.000-0.075)	79.6 (49.0-110.2)
	Synth+DAE	0.311 (0.204-0.417)	43.6 (22.9-64.2)
	Synth+PL	0.004 (0.000-0.040)	51.0 (20.7-81.2)
	Synth+UPL	0.000 (0.000-0.000)	256.0 (235.6-256.0)
	Synth+DPL	0.000 (0.000-0.001)	256.0 (226.8-256.0)
T2w	Baseline	0.000 (0.000-0.005)	62.7 (56.3-69.1)
	Baseline+TTA	0.000 (0.000-0.002)	63.1 (57.8-68.4)
	Baseline+TENT	0.000 (0.000-0.001)	85.7 (49.4-122.0)
	Baseline+DAE	0.000 (0.000-0.008)	69.8 (61.3-78.3)
	Baseline+PL	0.000 (0.000-0.002)	69.5 (62.8-76.2)
	Baseline+UPL	0.000 (0.000-0.000)	256.0 (256.0-256.0)
	Baseline+DPL	0.000 (0.000-0.000)	256.0 (256.0-256.0)
	Synth	0.111 (0.007-0.216)	75.0 (68.4-81.7)
	Synth+TTA	0.102 (0.000-0.211)	74.4 (68.0-80.8)
	Synth+TENT	0.105 (0.005-0.205)	70.7 (61.5-79.9)
	Synth+DAE	0.108 (0.000-0.218)	68.1 (58.0-78.1)
	Synth+PL	0.117 (0.004-0.230)	74.1 (67.4-80.8)
	Synth+UPL	0.004 (0.000-0.098)	63.7 (57.0-70.3)
	Synth+DPL	0.000 (0.000-0.076)	62.2 (52.6-71.8)
FLAIR	Baseline	0.000 (0.000-0.000)	65.8 (56.9-74.7)
	Baseline+TTA	0.000 (0.000-0.000)	71.8 (38.5-105.2)
	Baseline+TENT	0.000 (0.000-0.000)	92.4 (63.0-121.9)
	Baseline+DAE	0.000 (0.000-0.000)	79.0 (68.5-89.5)
	Baseline+PL	0.000 (0.000-0.000)	69.6 (54.5-84.7)
	Baseline+UPL	0.000 (0.000-0.000)	256.0 (256.0-256.0)
	Baseline+DPL	0.000 (0.000-0.000)	256.0 (256.0-256.0)
	Synth	0.212 (0.085-0.340)	56.1 (38.7-73.4)
	Synth+TTA	0.226 (0.097-0.355)	52.2 (19.1-85.3)
	Synth+TENT	0.000 (0.000-0.090)	71.0 (58.6-83.5)
	Synth+DAE	0.214 (0.099-0.329)	56.1 (47.3-64.9)
	Synth+PL	0.122 (0.004-0.240)	76.1 (64.2-87.9)
	Synth+UPL	0.000 (0.000-0.117)	71.6 (27.8-115.5)
	Synth+DPL	0.000 (0.000-0.111)	170.8 (126.7-214.8)
DWI	Baseline	0.000 (0.000-0.000)	73.1 (57.5-88.7)
	Baseline+TTA	0.000 (0.000-0.000)	83.7 (57.3-110.2)
	Baseline+TENT	0.000 (0.000-0.000)	84.3 (58.7-109.8)
	Baseline+DAE	0.000 (0.000-0.000)	70.5 (62.1-78.9)
	Baseline+PL	0.000 (0.000-0.006)	72.9 (65.1-80.8)
	Baseline+UPL	0.000 (0.000-0.000)	256.0 (256.0-256.0)
	Baseline+DPL	0.000 (0.000-0.000)	256.0 (256.0-256.0)
	Synth	0.056 (0.000-0.144)	84.9 (77.2-92.6)
	Synth+TTA	0.051 (0.000-0.145)	82.7 (75.2-90.2)
	Synth+TENT	0.000 (0.000-0.084)	78.4 (65.3-91.6)
	Synth+DAE	0.039 (0.000-0.132)	75.9 (68.4-83.5)
	Synth+PL	0.151 (0.068-0.234)	80.9 (74.4-87.5)
	Synth+UPL	0.038 (0.000-0.137)	71.5 (59.7-83.3)
	Synth+DPL	0.000 (0.000-0.069)	69.0 (30.4-107.6)
Ensemble	Baseline	0.000 (0.000-0.000)	256.0 (237.2-256.0)
	Baseline+TTA	0.000 (0.000-0.000)	256.0 (256.0-256.0)
	Baseline+TENT	0.000 (0.000-0.000)	256.0 (256.0-256.0)
	Baseline+DAE	0.000 (0.000-0.000)	256.0 (231.8-256.0)
	Baseline+PL	0.000 (0.000-0.000)	256.0 (223.0-256.0)
	Baseline+UPL	0.000 (0.000-0.000)	256.0 (256.0-256.0)
	Baseline+DPL	0.000 (0.000-0.000)	256.0 (256.0-256.0)
	Synth	0.423 (0.302-0.545)	47.3 (24.2-70.4)
	Synth+TTA	0.462 (0.338-0.586)	43.1 (12.2-74.0)
	Synth+TENT	0.000 (0.000-0.099)	66.9 (27.2-106.5)
	Synth+DAE	0.408 (0.288-0.528)	44.6 (25.0-64.1)
	Synth+PL	0.081 (0.000-0.187)	58.7 (50.0-67.4)
	Synth+UPL	0.000 (0.000-0.023)	256.0 (224.0-256.0)
	Synth+DPL	0.000 (0.000-0.037)	256.0 (216.4-256.0)

better reflects the likely use-case in a clinical setting, where data may be highly varied in the combinations of channels available at test-time. Strong performance on both the T1w data and the full ensemble could support a scenario where T1w data is used alone when available, and otherwise all other channels are combined in an ensemble.

Scores are also reported in Table 3 for all DA methods using both the baseline and Synth models. The baseline model still achieves the highest score in both Dice and HD95 for the near-domain T1w data, however there is no significant difference between the baseline and the Synth model for both metrics. For the Synth model, all modalities see benefit from a range of DA methods: for T1w, TTA leads to a slight increase in Dice while DAE leads to a slight improvement in HD95; for T2w, both DAE and PL lead to significant improvements over the standard Synth model in both Dice and HD95; for FLAIR, improvements in Dice are seen for PL, TENT and DAE with the greatest improvement from TENT (with statistical significance in Dice). For the ensemble of all individual modalities, improvements in Dice are observed for TTA and DAE with the greatest coming from DAE. This provides further evidence that the robust initial predictions of the Synth model enable optimisation with DA methods. Notably the pseudo-labelling methods have a much lower success rate. It is possible that, after improving initial predictions with one of the other DA methods, further improvements could be made by fine-tuning on DA-enhanced pseudo-labels. These methods may also require further tailoring to the relatively difficult task of brain lesion segmentation.

4.4 PLORAS

This dataset is intended to be the most challenging dataset included in this work and the most representative of real clinical data, with large diversity in acquisition setting and in slice thickness. For both available modalities, the Synth model outperforms the baseline with statistical significance in Dice both with and without TTA.

Results are reported for the dataset in Figure 3 and Table 4. In the T2 modality, only the DAE method leads to improvement over the regular Synth model, albeit without statistical significance. For the FLAIR images, both TTA and UPL lead to a slight improvement in Dice over the standard Synth model, again without any statistical significance. The DAE method leads to a significant improvement in HD95 but a degradation in Dice. In both modalities, no method leads to a significant improvement for the baseline model.

A number of samples are also visualised for this dataset in Figure 5, including the result of each DA technique. The first, second and fourth row are all examples where the baseline Dice score is zero and the Synth model’s Dice

Table 3: Median results on the ARC dataset (N=229). Best score shown in bold. Student’s *t* distribution 95% confidence intervals given in brackets.

Modality	Model	Dice	HD95
T1w	Baseline	0.752 (0.715-0.790)	8.6 (2.3-14.9)
	Baseline+TTA	0.752 (0.713-0.790)	8.8 (2.5-15.0)
	Baseline+TENT	0.000 (0.000-0.029)	105.3 (91.5-119.1)
	Baseline+DAE	0.710 (0.674-0.746)	12.1 (6.2-18.0)
	Baseline+PL	0.343 (0.311-0.375)	64.9 (60.5-69.3)
	Baseline+UPL	0.339 (0.299-0.379)	40.2 (28.8-51.6)
	Baseline+DPL	0.339 (0.301-0.377)	24.2 (15.3-33.1)
	Synth	0.723 (0.684-0.762)	11.0 (4.0-18.0)
	Synth+TTA	0.729 (0.690-0.768)	11.2 (4.5-17.9)
	Synth+TENT	0.676 (0.638-0.715)	13.6 (6.8-20.4)
	Synth+DAE	0.712 (0.676-0.747)	10.5 (5.5-15.5)
	Synth+PL	0.296 (0.261-0.332)	168.1 (162.1-174.0)
Synth+UPL	0.368 (0.332-0.405)	22.9 (14.2-31.6)	
Synth+DPL	0.234 (0.203-0.266)	21.2 (10.1-32.3)	
T2w	Baseline	0.004 (0.000-0.014)	74.2 (71.1-77.2)
	Baseline+TTA	0.000 (0.000-0.007)	74.4 (71.4-77.4)
	Baseline+TENT	0.000 (0.000-0.000)	111.5 (100.4-122.5)
	Baseline+DAE	0.000 (0.000-0.016)	77.1 (73.7-80.6)
	Baseline+PL	0.001 (0.000-0.004)	76.1 (73.1-79.0)
	Baseline+UPL	0.000 (0.000-0.000)	256.0 (256.0-256.0)
	Baseline+DPL	0.000 (0.000-0.000)	256.0 (256.0-256.0)
	Synth	0.268 (0.233-0.302)	64.0 (60.5-67.4)
	Synth+TTA	0.221 (0.186-0.257)	64.9 (61.4-68.4)
	Synth+TENT	0.159 (0.115-0.203)	54.1 (49.5-58.6)
	Synth+DAE	0.543 (0.501-0.585)	42.0 (37.8-46.3)
	Synth+PL	0.427 (0.395-0.458)	62.7 (59.5-65.8)
Synth+UPL	0.069 (0.052-0.087)	46.9 (43.5-50.3)	
Synth+DPL	0.016 (0.006-0.027)	49.0 (45.6-52.4)	
FLAIR	Baseline	0.120 (0.076-0.163)	63.0 (54.1-71.9)
	Baseline+TTA	0.122 (0.076-0.169)	58.5 (49.5-67.4)
	Baseline+TENT	0.000 (0.000-0.017)	153.6 (134.5-172.7)
	Baseline+DAE	0.124 (0.058-0.190)	41.5 (31.2-51.7)
	Baseline+PL	0.089 (0.064-0.115)	77.0 (69.4-84.5)
	Baseline+UPL	0.000 (0.000-0.000)	256.0 (256.0-256.0)
	Baseline+DPL	0.000 (0.000-0.000)	256.0 (256.0-256.0)
	Synth	0.141 (0.097-0.185)	52.2 (43.3-61.1)
	Synth+TTA	0.112 (0.068-0.155)	48.8 (39.6-57.9)
	Synth+TENT	0.361 (0.296-0.426)	44.3 (34.5-54.1)
	Synth+DAE	0.148 (0.087-0.209)	46.5 (37.0-56.1)
	Synth+PL	0.277 (0.236-0.318)	100.3 (91.9-108.7)
Synth+UPL	0.000 (0.000-0.014)	56.0 (36.5-75.5)	
Synth+DPL	0.000 (0.000-0.006)	103.3 (81.6-125.0)	
Ensemble	Baseline	0.034 (0.013-0.054)	40.4 (33.5-47.3)
	Baseline+TTA	0.012 (0.000-0.032)	48.5 (40.4-56.6)
	Baseline+TENT	0.000 (0.000-0.004)	256.0 (248.6-256.0)
	Baseline+DAE	0.117 (0.086-0.147)	38.7 (32.8-44.5)
	Baseline+PL	0.002 (0.000-0.007)	72.8 (69.7-75.9)
	Baseline+UPL	0.000 (0.000-0.000)	256.0 (256.0-256.0)
	Baseline+DPL	0.000 (0.000-0.000)	256.0 (256.0-256.0)
	Synth	0.602 (0.566-0.638)	20.1 (14.8-25.3)
	Synth+TTA	0.614 (0.578-0.650)	18.6 (13.4-23.8)
	Synth+TENT	0.518 (0.474-0.561)	18.1 (10.7-25.4)
	Synth+DAE	0.700 (0.663-0.738)	13.4 (8.9-18.0)
	Synth+PL	0.609 (0.575-0.643)	52.3 (47.7-57.0)
Synth+UPL	0.212 (0.184-0.241)	25.2 (15.9-34.5)	
Synth+DPL	0.109 (0.085-0.133)	31.2 (19.9-42.4)	

score is over 0.6. In the third row, the baseline Dice is also zero but the Synth model Dice is also lower with a score of 0.2. In this instance, the model has correctly identified the lesion but has also mislabelled a large number of false positives in other locations. In the use-case of interactive segmentation, such an output could easily be refined with click-interactions to remove false-positive objects in existing medical imaging software. The sample images show that TTA is the most conservative of the DA techniques,

whilst TENT/DAE provide a middle ground between this and the extreme changes observed under the various PL methods.

Table 4: Median results on the PLORAS dataset (N=263). Best score shown in bold. Student’s *t* distribution 95% confidence intervals given in brackets.

Modality	Model	Dice	HD95
T1	Baseline	0.000 (0.000-0.013)	80.5 (75.7-85.3)
	Baseline+TTA	0.000 (0.000-0.008)	78.4 (73.8-83.1)
	Baseline+TENT	0.000 (0.000-0.001)	80.2 (65.9-94.4)
	Baseline+DAE	0.000 (0.000-0.020)	85.1 (79.9-90.3)
	Baseline+PL	0.000 (0.000-0.003)	79.0 (74.4-83.6)
	Baseline+UPL	0.000 (0.000-0.000)	256.0 (256.0-256.0)
	Baseline+DPL	0.000 (0.000-0.000)	256.0 (256.0-256.0)
	Synth	0.068 (0.014-0.121)	73.4 (68.5-78.3)
	Synth+TTA	0.070 (0.014-0.125)	73.4 (68.0-78.8)
	Synth+TENT	0.029 (0.000-0.080)	78.2 (73.0-83.5)
	Synth+DAE	0.084 (0.024-0.144)	66.3 (60.1-72.5)
	Synth+PL	0.002 (0.000-0.031)	60.8 (53.0-68.7)
Synth+UPL	0.000 (0.000-0.009)	144.5 (124.5-164.4)	
Synth+DPL	0.000 (0.000-0.020)	75.9 (56.3-95.6)	
T2	Baseline	0.000 (0.000-0.003)	80.6 (78.0-83.2)
	Baseline+TTA	0.000 (0.000-0.002)	80.6 (77.5-83.8)
	Baseline+TENT	0.000 (0.000-0.002)	82.2 (72.7-91.6)
	Baseline+DAE	0.000 (0.000-0.007)	82.1 (79.1-85.2)
	Baseline+PL	0.000 (0.000-0.001)	83.0 (80.7-85.3)
	Baseline+UPL	0.000 (0.000-0.000)	256.0 (256.0-256.0)
	Baseline+DPL	0.000 (0.000-0.000)	256.0 (256.0-256.0)
	Synth	0.121 (0.088-0.154)	79.9 (76.8-82.9)
	Synth+TTA	0.129 (0.095-0.164)	77.6 (74.3-80.8)
	Synth+TENT	0.001 (0.000-0.034)	78.8 (71.4-86.3)
	Synth+DAE	0.044 (0.007-0.080)	71.6 (67.9-75.3)
	Synth+PL	0.103 (0.074-0.133)	91.3 (88.4-94.2)
Synth+UPL	0.152 (0.119-0.185)	79.6 (76.1-83.2)	
Synth+DPL	0.000 (0.000-0.015)	79.9 (68.2-91.5)	
FLAIR	Baseline	0.000 (0.000-0.003)	80.6 (78.0-83.2)
	Baseline+TTA	0.000 (0.000-0.002)	80.6 (77.5-83.8)
	Baseline+TENT	0.000 (0.000-0.002)	82.2 (72.7-91.6)
	Baseline+DAE	0.000 (0.000-0.007)	82.1 (79.1-85.2)
	Baseline+PL	0.000 (0.000-0.001)	83.0 (80.7-85.3)
	Baseline+UPL	0.000 (0.000-0.000)	256.0 (256.0-256.0)
	Baseline+DPL	0.000 (0.000-0.000)	256.0 (256.0-256.0)
	Synth	0.121 (0.088-0.154)	79.9 (76.8-82.9)
	Synth+TTA	0.129 (0.095-0.164)	77.6 (74.3-80.8)
	Synth+TENT	0.001 (0.000-0.034)	78.8 (71.4-86.3)
	Synth+DAE	0.044 (0.007-0.080)	71.6 (67.9-75.3)
	Synth+PL	0.103 (0.074-0.133)	91.3 (88.4-94.2)
Synth+UPL	0.152 (0.119-0.185)	79.6 (76.1-83.2)	
Synth+DPL	0.000 (0.000-0.015)	79.9 (68.2-91.5)	

4.5 Ablation: To mix or not to mix?

For all experiments shown thus far, the Synth model used a mix of both synthetic data and the real ATLAS dataset. In order to evaluate whether this decision is justified, an ablation is performed where the Synth model using mixed real/synthetic data is compared to a model trained with only synthetic data. This model is trained in the exact same manner as described previously for the baseline and Synth models. Results for the test datasets ATLAS, ISLES 2015 and ARC are shown in Tables 5, 6 and 7 respectively. In the in-domain ATLAS T1w data, the Synth model without mixed real data performs significantly worse than both the mixed data Synth model and the baseline model. In the ISLES 2015 dataset, the model without real data performs significantly better in Dice for the T1w modality. For all other modalities, there is no significant difference between the two Synth models in Dice score. Finally, in the ISLES dataset the model without any real data again performs significantly worse than both others in the near-domain T1w images. It does however perform significantly better than both others for the T2 data.

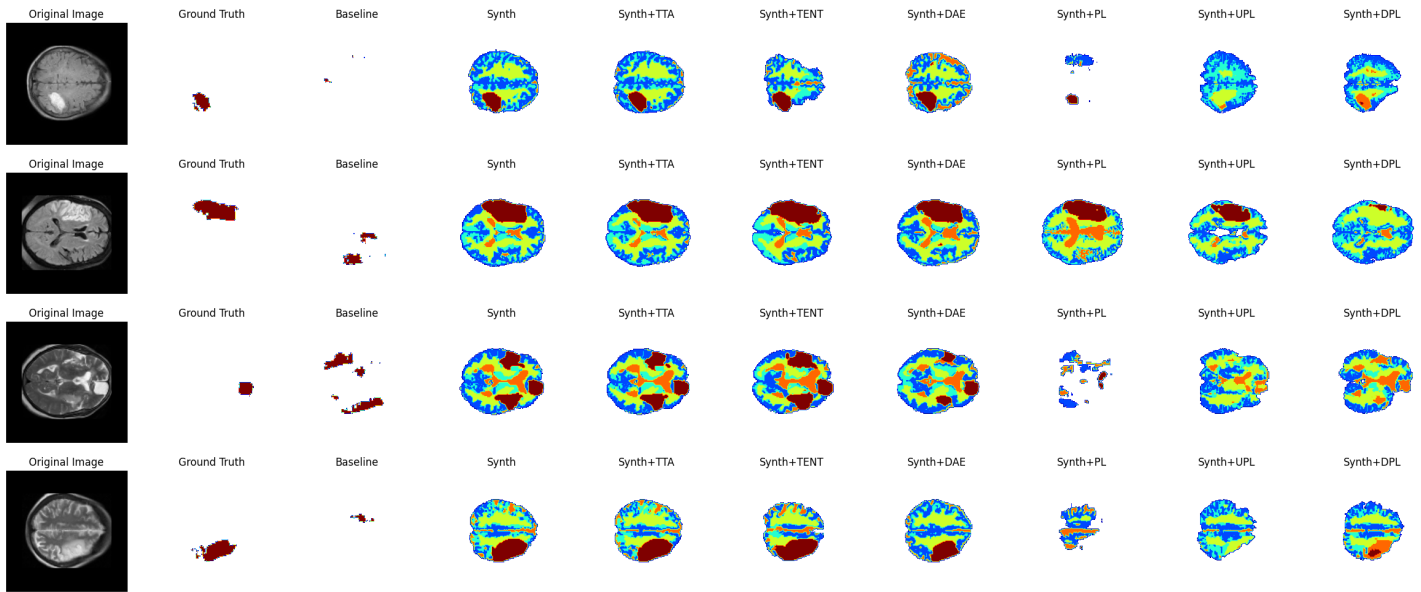


Figure 5: Sample visualisations in the PLORAS dataset.

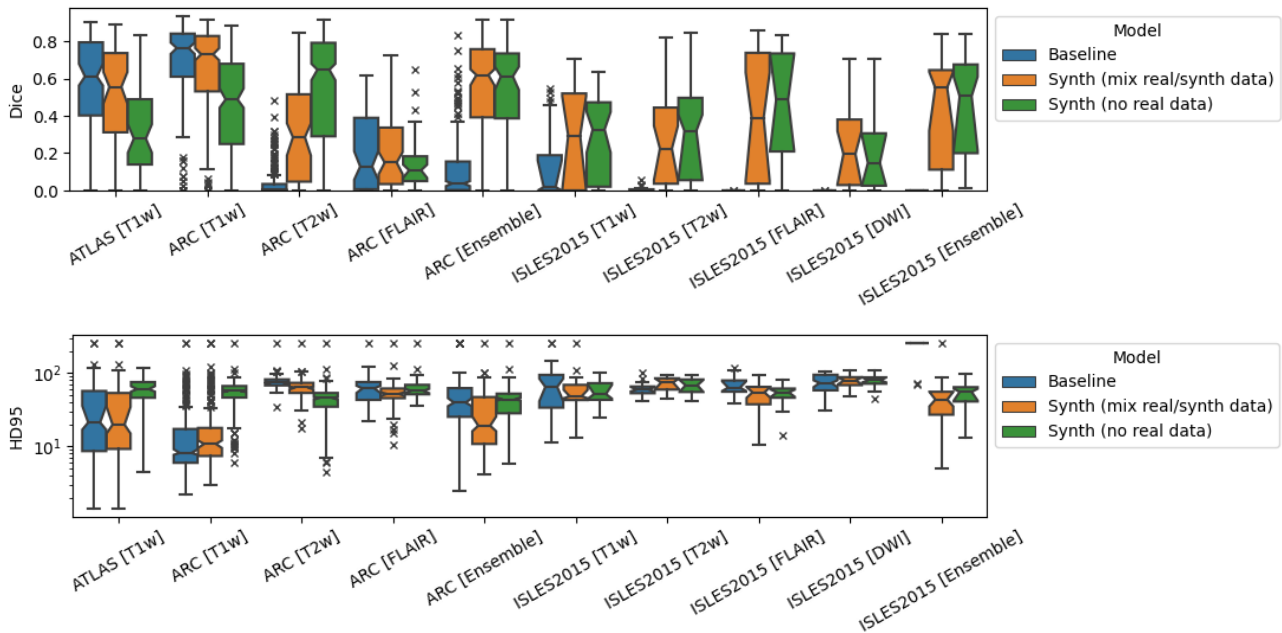


Figure 6: Dice and 95th-percentile Hausdorff Distance for all reported datasets, for models trained on different combinations of real/synthetic data.

Table 5: Median results for an ablation study on the ATLAS test set ($N=131$). Best score shown in bold. Student’s t distribution 95% confidence intervals given in brackets.

Modality	Model	Dice	HD95
T1w	Baseline	0.575 (0.523-0.627)	23.5 (13.9-33.2)
	Synth (no real data)	0.197 (0.155-0.239)	63.7 (59.6-67.9)
	Synth (mix real/synth data)	0.482 (0.431-0.534)	22.6 (12.0-33.3)

tion of MPRAGE volumes from the PLORAS study (Price et al., 2010). Results in Figure 7 and Tables 8, 9 and 10 demonstrate an overall positive effect of pseudo labels in the Synth model, with the ARC ensemble result seeing a statistically significant increase in Dice as a result of the new data. The in-domain ATLAS dataset also shows a notable improvement for both models as a result of pseudo labels, with a more marked increase in the baseline model.

4.6 Use of Pseudo-labelling

The use of synthetic data for semi-supervised pseudo-label training is also explored through the use of a large collec-

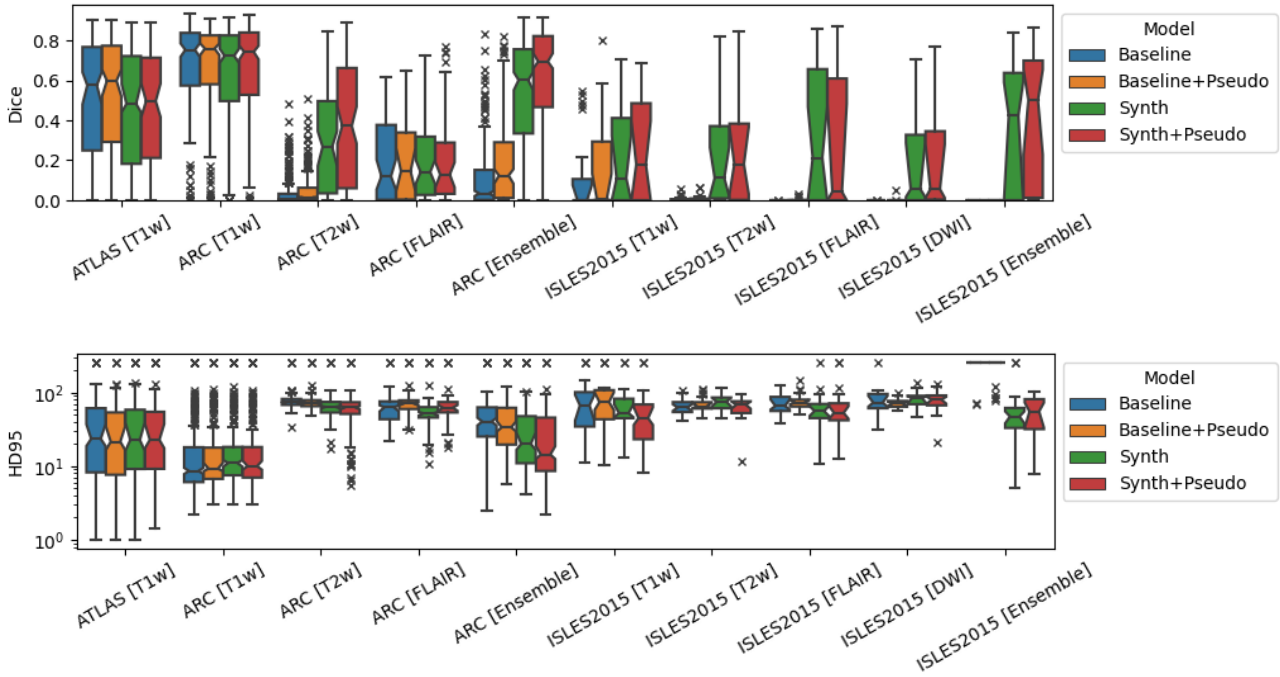


Figure 7: Dice and 95th-percentile Hausdorff Distance for all reported datasets, for models trained with/without an additional dataset of MPRAGE images and pseudo-labels.

Table 6: Median results for an ablation study on the ISLES 2015 test set (N=28). Best score shown in bold. Student’s t distribution 95% confidence intervals given in brackets.

Modality	Model	Dice	HD95
T1w	Baseline	0.000 (0.000-0.074)	67.0 (39.7-94.2)
	Synth (no real data)	0.304 (0.213-0.396)	58.6 (48.5-68.6)
	Synth (mix real/synth data)	0.110 (0.012-0.208)	52.5 (29.9-75.0)
T2w	Baseline	0.000 (0.000-0.005)	62.7 (56.3-69.1)
	Synth (no real data)	0.074 (0.000-0.184)	72.3 (65.7-78.9)
	Synth (mix real/synth data)	0.111 (0.007-0.216)	75.0 (68.4-81.7)
FLAIR	Baseline	0.000 (0.000-0.000)	65.8 (56.9-74.7)
	Synth (no real data)	0.372 (0.255-0.489)	56.1 (49.5-62.7)
	Synth (mix real/synth data)	0.212 (0.085-0.340)	56.1 (38.7-73.4)
DWI	Baseline	0.000 (0.000-0.000)	73.1 (57.5-88.7)
	Synth (no real data)	0.082 (0.000-0.168)	83.7 (76.3-91.0)
	Synth (mix real/synth data)	0.056 (0.000-0.144)	84.9 (77.2-92.6)
Ensemble	Baseline	0.000 (0.000-0.000)	256.0 (237.2-256.0)
	Synth (no real data)	0.272 (0.157-0.388)	60.1 (49.7-70.5)
	Synth (mix real/synth data)	0.423 (0.302-0.545)	47.3 (24.2-70.4)

Table 7: Median results for an ablation study on the ARC test set (N=229). Best score shown in bold. Student’s t distribution 95% confidence intervals given in brackets.

Modality	Model	Dice	HD95
T1w	Baseline	0.752 (0.715-0.790)	8.6 (2.3-14.9)
	Synth (no real data)	0.467 (0.430-0.504)	57.1 (52.9-61.3)
	Synth (mix real/synth data)	0.723 (0.684-0.762)	11.0 (4.0-18.0)
T2w	Baseline	0.004 (0.000-0.014)	74.2 (71.1-77.2)
	Synth (no real data)	0.626 (0.588-0.665)	46.1 (42.2-50.0)
	Synth (mix real/synth data)	0.268 (0.233-0.302)	64.0 (60.5-67.4)
FLAIR	Baseline	0.120 (0.076-0.163)	63.0 (54.1-71.9)
	Synth (no real data)	0.096 (0.070-0.123)	57.6 (49.2-65.9)
	Synth (mix real/synth data)	0.141 (0.097-0.185)	52.2 (43.3-61.1)
Ensemble	Baseline	0.034 (0.013-0.054)	40.4 (33.5-47.3)
	Synth (no real data)	0.597 (0.562-0.631)	44.0 (39.9-48.2)
	Synth (mix real/synth data)	0.602 (0.566-0.638)	20.1 (14.8-25.3)

Table 8: Median results with and without pseudo-label training on the ATLAS test set (N=131). Best score shown in bold. Student’s t distribution 95% confidence intervals given in brackets.

Modality	Model	Dice	HD95
T1w	Baseline	0.575 (0.523-0.627)	23.5 (13.9-33.2)
	Baseline+Pseudo	0.598 (0.548-0.647)	21.5 (13.8-29.1)
	Synth	0.482 (0.431-0.534)	22.6 (12.0-33.3)
	Synth+Pseudo	0.496 (0.445-0.547)	22.8 (11.5-34.1)

5. Conclusion

In this study, we introduced a novel synthetic data generation and training framework for stroke lesion segmentation, building on the success of prior works in healthy brain parcellation. A model trained using this novel framework was evaluated on a wide range of datasets covering research and clinical data, and chronic and acute stroke pathologies. Results demonstrated that the proposed model is on par with the state-of-the-art for in-domain MPRAGE data, whilst being able to significantly outperform the state-of-the-art model in a variety of out-of-domain scenarios. This was further supported by comparison to a number of state-of-the-art domain adaptation techniques. These domain adaptation techniques consistently led to improvements from the base prediction of our new model, whilst degrading the already poor performance of the MPRAGE-trained model in all scenarios. This provides evidence for the value of our model as a robust ‘one size fits all’ base model that can provide an excellent initial prediction with which to adapt

Table 9: Median results with and without pseudo-label training on the ISLES 2015 test set (N=28). Best score shown in bold. Student's t distribution 95% confidence intervals given in brackets.

Modality	Model	Dice	HD95
T1w	Baseline	0.000 (0.000-0.074)	67.0 (39.7-94.2)
	Baseline+Pseudo	0.003 (0.000-0.091)	74.2 (48.3-100.0)
	Synth	0.110 (0.012-0.208)	52.6 (30.0-75.1)
	Synth+Pseudo	0.179 (0.076-0.283)	44.8 (20.9-68.8)
T2w	Baseline	0.000 (0.000-0.005)	62.7 (56.3-69.1)
	Baseline+Pseudo	0.001 (0.000-0.007)	64.9 (58.3-71.5)
	Synth	0.111 (0.007-0.216)	75.0 (68.4-81.7)
	Synth+Pseudo	0.181 (0.071-0.291)	68.3 (61.1-75.4)
FLAIR	Baseline	0.000 (0.000-0.000)	65.8 (56.9-74.7)
	Baseline+Pseudo	0.000 (0.000-0.003)	73.3 (65.4-81.3)
	Synth	0.212 (0.085-0.340)	56.1 (38.7-73.4)
	Synth+Pseudo	0.042 (0.000-0.173)	52.9 (30.4-75.4)
DWI	Baseline	0.000 (0.000-0.000)	73.1 (57.5-88.7)
	Baseline+Pseudo	0.000 (0.000-0.004)	71.6 (67.5-75.7)
	Synth	0.056 (0.000-0.144)	84.9 (77.2-92.6)
	Synth+Pseudo	0.056 (0.000-0.147)	80.4 (71.6-89.2)
Ensemble	Baseline	0.000 (0.000-0.000)	256.0 (237.2-256.0)
	Baseline+Pseudo	0.000 (0.000-0.000)	256.0 (231.1-256.0)
	Synth	0.423 (0.302-0.545)	47.3 (24.2-70.4)
	Synth+Pseudo	0.501 (0.376-0.626)	55.3 (43.7-67.0)

Table 10: Median results with and without pseudo-label training on the ARC test set (N=229). Best score shown in bold. Student's t distribution 95% confidence intervals given in brackets.

Modality	Model	Dice	HD95
T1w	Baseline	0.752 (0.715-0.790)	8.6 (2.3-14.9)
	Baseline+Pseudo	0.759 (0.721-0.797)	9.3 (3.8-14.7)
	Synth	0.723 (0.684-0.762)	11.0 (4.0-18.0)
	Synth+Pseudo	0.743 (0.704-0.782)	10.0 (3.3-16.7)
T2w	Baseline	0.004 (0.000-0.014)	74.2 (71.1-77.2)
	Baseline+Pseudo	0.014 (0.003-0.024)	72.1 (69.0-75.1)
	Synth	0.268 (0.233-0.302)	64.0 (60.5-67.4)
	Synth+Pseudo	0.372 (0.332-0.411)	63.1 (59.2-66.9)
FLAIR	Baseline	0.120 (0.076-0.163)	63.0 (54.1-71.9)
	Baseline+Pseudo	0.145 (0.101-0.189)	70.6 (62.4-78.8)
	Synth	0.141 (0.097-0.185)	52.2 (43.3-61.1)
	Synth+Pseudo	0.129 (0.084-0.173)	62.1 (53.5-70.7)
Ensemble	Baseline	0.034 (0.013-0.054)	40.4 (33.5-47.3)
	Baseline+Pseudo	0.124 (0.097-0.150)	33.7 (28.8-38.6)
	Synth	0.602 (0.566-0.638)	20.1 (14.8-25.3)
	Synth+Pseudo	0.694 (0.658-0.730)	14.4 (9.9-18.9)

or fine-tune to a new domain.

Qualitative investigation also demonstrates the potential of the model for a starting checkpoint in an active-learning framework such as MONAI Label (Diaz-Pinto et al., 2024) where predictions may be refined to generate training data for task-specific fine-tuning. The uncertainty of healthy-tissue segmentations via MC dropout may also provide an effective heuristic for prioritising items to refine/label in such a framework (Nath et al., 2021).

Results also showed the potential benefit of the model for semi-supervised learning through pseudo labelling, where predicted labels may be fed back into the model with much less caution than is typically required when training with

real images (Pham et al., 2021; Xu et al., 2024). A simple solution to further reinforce this may be to train a real/fake discriminator to perform automated quality-control and threshold optimisation for the generated binary maps.

Although results in the paper provide strong evidence of the raw value of the segmentation metrics, it is important to further validate that the predictions made from the trained model are useful for downstream tasks. This could be validated by comparing predictivity of the segmentation masks for functional scores such as the Comprehensive Aphasia Test (CAT) (Hope et al., 2024) or the NIH Stroke Score (NIHSS).

While this study focused on stroke, the results are expected to translate to other similar domains, such as haemorrhage and glioblastoma. Future work will compare the impact of the mixing proportions of real and synthetic data. Additionally, the utility of multi-modal data in a multi-channel model will be examined versus post-hoc averaging of individual modality predictions. Lesions often appear differently across modalities, so a model trained with multi-channel inputs is expected to leverage these differences more effectively. This relationship between multi-channel inputs may better be modelled using quantitative MRI data.

In the context of neuroimaging data, there are many shifts in domain beyond those related to scanner sequence and resolution targeted in this work. Shifts related to anatomical shape, brought on by changes in demographics or the presence of confounding conditions such as atrophy are of equal importance to shifts in image appearance. Prior work has attempted to model such factors through the use of causal inference and counterfactual generation (Pawlowski et al., 2020; Pombo et al., 2023; Ribeiro et al., 2023). It is conceivable that such an approach could be used to introduce morphological changes to the healthy tissue maps to create a model that is agnostic to shifts in domains related to both shape and appearance.

Acknowledgments

LC is supported by the EPSRC-funded UCL Centre for Doctoral Training in Intelligent, Integrated Imaging in Healthcare (i4health) (EP/S021930/1), and the Wellcome Trust (203147/Z/16/Z and 205103/Z/16/Z). IP supported by the Alzheimer's Association grant number SG-20-678486-GAAIN2. This research was supported by NVIDIA and utilized NVIDIA RTX A6000 48GB.

Ethical Standards

The work follows appropriate ethical standards in conduct-

ing research and writing the manuscript, following all applicable laws and regulations regarding treatment of animals or human subjects.

Conflicts of Interest

We declare we don't have conflicts of interest.

Data availability

Authors have released public code and weights to reimplement all experiments. Model weights are also made available as a toolbox for SPM. This toolbox is written in pure MATLAB and requires no external installs or compilation, to minimise the barrier for clinical evaluation. All datasets are public except the PLORAS study data, which is part of an ongoing study and will be published upon completion.

References

- John Ashburner and Karl J. Friston. Unified segmentation. *NeuroImage*, 26(3):839–851, 2005. ISSN 10538119. .
- Ujjwal Baid, Satyam Ghodasara, Suyash Mohan, and others. The RSNA-ASNR-MICCAI BraTS 2021 Benchmark on Brain Tumor Segmentation and Radiogenomic Classification, 2021.
- Benjamin Billot, Stefano Cerri, Koen Van Leemput, Adrian V. Dalca, and Juan Eugenio Iglesias. Joint segmentation of multiple sclerosis lesions and brain anatomy in MRI scans of any contrast and resolution with CNNs. In *2021 IEEE 18th International Symposium on Biomedical Imaging (ISBI)*. IEEE, April 2021. .
- Benjamin Billot, Douglas N. Greve, Oula Puonti, Axel Thielscher, Koen Van Leemput, Bruce Fischl, Adrian V. Dalca, and Juan Eugenio Iglesias. SynthSeg: Segmentation of brain MRI scans of any contrast and resolution without retraining. *Medical Image Analysis*, 86:102789, May 2023. ISSN 1361-8415. .
- Mikael Brudfors, Yaël Balbastre, Guillaume Flandin, Parashkev Nachev, and John Ashburner. *Flexible Bayesian Modelling for Nonlinear Image Registration*, page 253–263. Springer International Publishing, 2020. ISBN 9783030597160. .
- M. Jorge Cardoso, Wenqi Li, Richard Brown, Nic Ma, Eric Kerfoot, Yiheng Wang, Benjamin Murrey, Andriy Myronenko, Can Zhao, Dong Yang, Vishwesh Nath, Yufan He, Ziyue Xu, Ali Hatamizadeh, Andriy Myronenko, Wentao Zhu, Yun Liu, Mingxin Zheng, Yucheng Tang, Isaac Yang, Michael Zephyr, Behrooz Hashemian, Sachidanand Alle, Mohammad Zalbagi Darestani, Charlie Budd, Marc Modat, Tom Vercauteren, Guotai Wang, Yiwen Li, Yipeng Hu, Yunguan Fu, Benjamin Gorman, Hans Johnson, Brad Genereaux, Barbaros S. Erdal, Vikash Gupta, Andres Diaz-Pinto, Andre Dourson, Lena Maier-Hein, Paul F. Jaeger, Michael Baumgartner, Jayashree Kalpathy-Cramer, Mona Flores, Justin Kirby, Lee A. D. Cooper, Holger R. Roth, Daguang Xu, David Bericat, Ralf Floca, S. Kevin Zhou, Haris Shuaib, Keyvan Farahani, Klaus H. Maier-Hein, Stephen Aylward, Prerna Dogra, Sebastien Ourselin, and Andrew Feng. Monai: An open-source framework for deep learning in healthcare, 2022.
- Stefano Cerri, Oula Puonti, Dominik S. Meier, Jens Wuerfel, Mark Mühlau, Hartwig R. Siebner, and Koen Van Leemput. A contrast-adaptive method for simultaneous whole-brain and lesion segmentation in multiple sclerosis. *NeuroImage*, 225:117471, January 2021. ISSN 1053-8119. .
- Cheng Chen, Quande Liu, Yueming Jin, Qi Dou, and Pheng-Ann Heng. Source-free domain adaptive fundus image segmentation with denoised pseudo-labeling, 2021. URL <https://arxiv.org/abs/2109.09735>.
- Etienne Chollet, Yaël Balbastre, Chiara Mauri, Caroline Magnain, Bruce Fischl, and Hui Wang. Neurovascular segmentation in soct with deep learning and synthetic training data, 2024. URL <https://arxiv.org/abs/2407.01419>.
- Pingping Dai, Licong Dong, Ruihan Zhang, Haiming Zhu, Jie Wu, and Kehong Yuan. Soft-CP: A credible and effective data augmentation for semantic segmentation of medical lesions, 2022.
- Adrian V. Dalca, John Guttag, and Mert R. Sabuncu. Anatomical priors in convolutional networks for unsupervised biomedical segmentation. In *2018 IEEE/CVF Conference on Computer Vision and Pattern Recognition*. IEEE, June 2018. .
- Ezequiel de la Rosa, Mauricio Reyes, Sook-Lei Liew, Alexandre Hutton, Roland Wiest, Johannes Kaesmacher, Uta Hanning, Arsany Hakim, Richard Zubal, Waldo Valenzuela, David Robben, Diana M. Sima, Vincenzo Anania, Arne Brys, James A. Meakin, Anne Mickan, Gabriel Broocks, Christian Heitkamp, Shengbo Gao, Kongming Liang, Ziji Zhang, Md Mahfuzur Rahman Siddiquee, Andriy Myronenko, Pooya Ashtari, Sabine Van Huffel, Hyun su Jeong, Chi ho Yoon, Chulhong Kim, Jiayu Huo, Sebastien Ourselin, Rachel Sparks, Albert Clèrigues, Arnau Oliver, Xavier Lladó, Liam Chalcraft, Ioannis Pappas, Jeroen Bertels, Ewout Heylen, Juliette

- Moreau, Nima Hatami, Carole Frindel, Abdul Qayyum, Moona Mazher, Domenec Puig, Shao-Chieh Lin, Chun-Jung Juan, Tianxi Hu, Lyndon Boone, Maged Goubran, Yi-Jui Liu, Susanne Wegener, Florian Kofler, Ivan Ezhov, Suprosanna Shit, Moritz R. Hernandez Petzsche, Bjoern Menze, Jan S. Kirschke, and Benedikt Wiestler. A robust ensemble algorithm for ischemic stroke lesion segmentation: Generalizability and clinical utility beyond the isles challenge, 2024. URL <https://arxiv.org/abs/2403.19425>.
- Andres Diaz-Pinto, Sachidanand Alle, Vishwesh Nath, Yucheng Tang, Alvin Ihsani, Muhammad Asad, Fernando Pérez-García, Pritesh Mehta, Wenqi Li, Mona Flores, Holger R. Roth, Tom Vercauteren, Daguang Xu, Prerna Dogra, Sebastien Ourselin, Andrew Feng, and M. Jorge Cardoso. Monai label: A framework for ai-assisted interactive labeling of 3d medical images. *Medical Image Analysis*, 95:103207, July 2024. ISSN 1361-8415. . URL <http://dx.doi.org/10.1016/j.media.2024.103207>.
- Yarin Gal and Zoubin Ghahramani. Dropout as a bayesian approximation: Representing model uncertainty in deep learning. In Maria Florina Balcan and Kilian Q. Weinberger, editors, *Proceedings of The 33rd International Conference on Machine Learning*, volume 48 of *Proceedings of Machine Learning Research*, pages 1050–1059, New York, New York, USA, 20–22 Jun 2016. PMLR. URL <https://proceedings.mlr.press/v48/gal16.html>.
- Makayla Gibson, Roger Newman-Norlund, Leonardo Bonilha, Julius Fridriksson, Gregory Hickok, Argye E. Hillis, Dirk Bart den Ouden, and Christopher Rorden. The Aphasia Recovery Cohort, an open-source chronic stroke repository. *Scientific Data*, 11(1):1–8, 2024. ISSN 20524463. . URL <http://dx.doi.org/10.1038/s41597-024-03819-7>.
- Karthik Gopinath, Douglas N. Greve, Sudeshna Das, Steve Arnold, Colin Magdamo, and Juan Eugenio Iglesias. Cortical analysis of heterogeneous clinical brain mri scans for large-scale neuroimaging studies, 2023. URL <https://arxiv.org/abs/2305.01827>.
- Karthik Gopinath, Douglas N. Greve, Colin Magdamo, Steve Arnold, Sudeshna Das, Oula Puonti, and Juan Eugenio Iglesias. Recon-all-clinical: Cortical surface reconstruction and analysis of heterogeneous clinical brain mri, 2024a. URL <https://arxiv.org/abs/2409.03889>.
- Karthik Gopinath, Andrew Hoopes, Daniel C. Alexander, Steven E. Arnold, Yael Balbastre, Adrià Casamitjana, You Cheng, Russ Yue Zhi Chua, Brian L. Edlow, Bruce Fischl, Harshvardhan Gazula, Malte Hoffmann, C. Dirk Keene, Seunghoi Kim, W. Taylor Kimberly, Sonia Laguna, Kathleen E. Larson, Koen Van Leemput, Oula Puonti, Livia M. Rodrigues, Matthew S. Rosen, Henry F. J. Tregidgo, Divya Varadarajan, Sean I. Young, Adrian V. Dalca, and Juan Eugenio Iglesias. Synthetic data in generalizable, learning-based neuroimaging. *Imaging Neuroscience*, 2024b. ISSN 2837-6056. . URL http://dx.doi.org/10.1162/imag_a_00337.
- Kaiming He, Xiangyu Zhang, Shaoqing Ren, and Jian Sun. Delving deep into rectifiers: Surpassing human-level performance on ImageNet classification, 2015.
- Malte Hoffmann, Benjamin Billot, Douglas N Greve, Juan Eugenio Iglesias, Bruce Fischl, and Adrian V Dalca. Synthmorph: learning contrast-invariant registration without acquired images. *IEEE Transactions on Medical Imaging*, 41(3):543–558, 2022.
- Malte Hoffmann, Andrew Hoopes, Bruce Fischl, and Adrian V Dalca. Anatomy-specific acquisition-agnostic affine registration learned from fictitious images. In *Medical Imaging 2023: Image Processing*, volume 12464, page 1246402. SPIE, 2023.
- Malte Hoffmann, Andrew Hoopes, Douglas N Greve, Bruce Fischl, and Adrian V Dalca. Anatomy-aware and acquisition-agnostic joint registration with synthmorph. *Imaging Neuroscience*, 2:1–33, 2024.
- Thomas M.H. Hope, Douglas Neville, Mohamed L. Seghier, and Cathy J. Price. Continuous lesion images drive more accurate predictions of outcomes after stroke than binary lesion images. October 2024. . URL <http://dx.doi.org/10.1101/2024.10.04.616726>.
- Juan E. Iglesias, Benjamin Billot, Yaël Balbastre, Colin Magdamo, Steven E. Arnold, Sudeshna Das, Brian L. Edlow, Daniel C. Alexander, Polina Golland, and Bruce Fischl. Synthsr: A public ai tool to turn heterogeneous clinical brain scans into high-resolution t1-weighted images for 3d morphometry. *Science Advances*, 9(5), February 2023. ISSN 2375-2548. . URL <http://dx.doi.org/10.1126/sciadv.add3607>.
- Juan Eugenio Iglesias, Benjamin Billot, Yaël Balbastre, Azadeh Tabari, John Conklin, R. Gilberto González, Daniel C. Alexander, Polina Golland, Brian L. Edlow, and Bruce Fischl. Joint super-resolution and synthesis of 1 mm isotropic MP-RAGE volumes from clinical MRI exams with scans of different orientation, resolution and contrast. *NeuroImage*, 237, 2021.
- Fabian Isensee, Paul F. Jaeger, Simon A. A. Kohl, Jens Petersen, and Klaus H. Maier-Hein. nnU-Net: a self-configuring method for deep learning-based biomedical

- image segmentation. *Nature Methods*, 18(2):203–211, December 2020. ISSN 1548-7105. .
- Fabian Isensee, Tassilo Wald, Constantin Ulrich, Michael Baumgartner, Saikat Roy, Klaus Maier-Hein, and Paul F. Jaeger. nnu-net revisited: A call for rigorous validation in 3d medical image segmentation, 2024. URL <https://arxiv.org/abs/2404.09556>.
- Lisa Johnson, Roger Newman-Norlund, Alex Teghipco, et al. Progressive lesion necrosis is related to increasing aphasia severity in chronic stroke. *NeuroImage: Clinical*, 41, 1 2024. ISSN 22131582. .
- Neerav Karani, Ertunc Erdil, Krishna Chaitanya, and Ender Konukoglu. Test-time adaptable neural networks for robust medical image segmentation. *Medical Image Analysis*, 68:101907, February 2021. ISSN 1361-8415. . URL <http://dx.doi.org/10.1016/j.media.2020.101907>.
- Pamela J. LaMontagne, Tammie LS. Benzinger, John C. Morris, Sarah Keefe, Russ Hornbeck, Chengjie Xiong, Elizabeth Grant, Jason Hassenstab, Krista Moulder, Andrei G. Vlassenko, Marcus E. Raichle, Carlos Cruchaga, and Daniel Marcus. OASIS-3: Longitudinal neuroimaging, clinical, and cognitive dataset for normal aging and Alzheimer disease. *medRxiv*, December 2019. .
- Hans Lassmann. Multiple sclerosis pathology. *Cold Spring Harbor Perspectives in Medicine*, 8(3):a028936, January 2018. ISSN 2157-1422. .
- Sook-Lei Liew, Bethany P. Lo, Miranda R. Donnelly, Artemis Zavaliangos-Petropulu, Jessica N. Jeong, Giuseppe Barisano, Alexandre Hutton, Julia P. Simon, Julia M. Juliano, Anisha Suri, Zhizhuo Wang, Aisha Abdullah, Jun Kim, Tyler Ard, Nerisa Banaj, Michael R. Borich, Lara A. Boyd, Amy Brodtmann, Cathrin M. Buetefisch, Lei Cao, Jessica M. Cassidy, Valentina Ciullo, Adriana B. Conforto, Steven C. Cramer, Rosalia Dacosta-Aguayo, Ezequiel de la Rosa, Martin Domin, Adrienne N. Dula, Wuwei Feng, Alexandre R. Franco, Fatemeh Geranmayeh, Alexandre Gramfort, Chris M. Gregory, Colleen A. Hanlon, Brenton G. Hordacre, Steven A. Kautz, Mohamed Salah Khlif, Hosung Kim, Jan S. Kirschke, Jingchun Liu, Martin Lotze, Bradley J. MacIntosh, Maria Mataró, Feroze B. Mohamed, Jan E. Nordvik, Gilsoon Park, Amy Pienta, Fabrizio Piras, Shane M. Redman, Kate P. Revill, Mauricio Reyes, Andrew D. Robertson, Na Jin Seo, Surjo R. Soekadar, Gianfranco Spalletta, Alison Sweet, Maria Telenczuk, Gregory Thielman, Lars T. Westlye, Carolee J. Winstein, George F. Wittenberg, Kristin A. Wong, and Chunshui Yu. A large, curated, open-source stroke neuroimaging dataset to improve lesion segmentation algorithms. *Scientific Data*, 9(1), June 2022. ISSN 2052-4463. .
- Peirong Liu, Oula Puonti, Annabel Sorby-Adams, William T. Kimberly, and Juan E. Iglesias. PEPSI: Pathology-Enhanced Pulse-Sequence-Invariant Representations for Brain MRI, 3 2024. URL <http://arxiv.org/abs/2403.06227>.
- Ilya Loshchilov and Frank Hutter. Decoupled weight decay regularization, 2019.
- Robert Loughnan, Diego L. Lorca-Puls, Andrea Gajardo-Vidal, Valeria Espejo-Videla, Céline R. Gillebert, Dante Mantini, Cathy J. Price, and Thomas M.H. Hope. Generalizing post-stroke prognoses from research data to clinical data. *NeuroImage: Clinical*, 24(October 2019): 102005, 2019. ISSN 22131582. . URL <https://doi.org/10.1016/j.nicl.2019.102005>.
- Oskar Maier, Bjoern H. Menze, Janina von der Gablentz, Levin Häni, Mattias P. Heinrich, Matthias Liebrand, Stefan Winzeck, Abdul Basit, Paul Bentley, Liang Chen, Daan Christiaens, Francis Dutil, Karl Egger, Chaolu Feng, Ben Glocker, Michael Götz, Tom Haeck, Hanna-Leena Halme, Mohammad Havaei, Khan M. Iftekharuddin, Pierre-Marc Jodoin, Konstantinos Kamnitsas, Elias Kellner, Antti Korvenoja, Hugo Larochelle, Christian Ledig, Jia-Hong Lee, Frederik Maes, Qaiser Mahmood, Klaus H. Maier-Hein, Richard McKinley, John Muschelli, Chris Pal, Linmin Pei, Janaki Raman Rangarajan, Syed M.S. Reza, David Robben, Daniel Rueckert, Eero Salli, Paul Suetens, Ching-Wei Wang, Matthias Wilms, Jan S. Kirschke, Ulrike M. Krämer, Thomas F. Münte, Peter Schramm, Roland Wiest, Heinz Handels, and Mauricio Reyes. ISLES 2015 - a public evaluation benchmark for ischemic stroke lesion segmentation from multispectral MRI. *Medical Image Analysis*, 35:250–269, January 2017. ISSN 1361-8415. .
- Jon Middleton, Marko Bauer, Kaining Sheng, Jacob Johansen, Mathias Perslev, Silvia Ingala, Mads Nielsen, and Akshay Pai. Local gamma augmentation for ischemic stroke lesion segmentation on mri, 2024. URL <https://arxiv.org/abs/2401.06893>.
- Vishwesh Nath, Dong Yang, Bennett A. Landman, Daguang Xu, and Holger R. Roth. Diminishing uncertainty within the training pool: Active learning for medical image segmentation. *IEEE Transactions on Medical Imaging*, 40(10):2534–2547, October 2021. ISSN 1558-254X. . URL <http://dx.doi.org/10.1109/TMI.2020.3048055>.
- Thanh N Nguyen, Mohamad Abdalkader, Urs Fischer, Zhongming Qiu, Simon Nagel, Hui-Sheng Chen, Zhon-

- grong Miao, and Pooja Khatri. Endovascular management of acute stroke. *The Lancet*, 404(10459): 1265–1278, September 2024. ISSN 0140-6736. URL [http://dx.doi.org/10.1016/S0140-6736\(24\)01410-7](http://dx.doi.org/10.1016/S0140-6736(24)01410-7).
- Nick Pawlowski, Daniel C. Castro, and Ben Glocker. Deep structural causal models for tractable counterfactual inference, 2020. URL <https://arxiv.org/abs/2006.06485>.
- Hieu Pham, Zihang Dai, Qizhe Xie, Minh-Thang Luong, and Quoc V. Le. Meta pseudo labels, 2021. URL <https://arxiv.org/abs/2003.10580>.
- Guilherme Pombo, Robert Gray, M Jorge Cardoso, Sébastien Ourselin, Geraint Rees, John Ashburner, and Parashkev Nachev. Equitable modelling of brain imaging by counterfactual augmentation with morphologically constrained 3D deep generative models. *Med. Image Anal.*, 84(102723):102723, February 2023.
- Cathy J. Price, Mohamed L. Seghier, and Alex P. Leff. Predicting language outcome and recovery after stroke: The PLORAS system. *Nature Reviews Neurology*, 6(4): 202–210, 2010. ISSN 17594758.
- Oula Puonti, Juan Eugenio Iglesias, and Koen Van Leemput. Fast and sequence-adaptive whole-brain segmentation using parametric Bayesian modeling. *NeuroImage*, 143:235–249, 2016. ISSN 10959572. URL <http://dx.doi.org/10.1016/j.neuroimage.2016.09.011>.
- Fabio De Sousa Ribeiro, Tian Xia, Miguel Monteiro, Nick Pawlowski, and Ben Glocker. High fidelity image counterfactuals with probabilistic causal models, 2023. URL <https://arxiv.org/abs/2306.15764>.
- Olaf Ronneberger, Philipp Fischer, and Thomas Brox. U-net: Convolutional networks for biomedical image segmentation, 2015.
- Mohamed L. Seghier, Anil Ramlackhansingh, Jenny Crinion, Alexander P. Leff, and Cathy J. Price. Lesion identification using unified segmentation-normalisation models and fuzzy clustering. *NeuroImage*, 41(4):1253–1266, 2008. ISSN 10538119. URL <http://dx.doi.org/10.1016/j.neuroimage.2008.03.028>.
- Mohamed L. Seghier, Elnas Patel, Susan Prejawa, Sue Ramsden, Andre Selmer, Louise Lim, Rachel Browne, Johanna Rae, Zula Haigh, Deborah Ezekiel, Thomas M.H. Hope, Alex P. Leff, and Cathy J. Price. The PLORAS Database: A data repository for Predicting Language Outcome and Recovery After Stroke. *NeuroImage*, 124:1208–1212, 2016. ISSN 10959572. URL <http://dx.doi.org/10.1016/j.neuroimage.2015.03.083>.
- Claude E. Shannon. A Mathematical Theory of Communication. *Bell System Technical Journal*, 27(3):379–423, 1948. ISSN 15387305.
- Dequan Wang, Evan Shelhamer, Shaoteng Liu, Bruno Olshausen, and Trevor Darrell. Tent: Fully test-time adaptation by entropy minimization, 2021.
- Guotai Wang, Wenqi Li, Sébastien Ourselin, and Tom Vercauteren. *Automatic Brain Tumor Segmentation Using Convolutional Neural Networks with Test-Time Augmentation*, page 61–72. Springer International Publishing, 2019. ISBN 9783030117269. URL http://dx.doi.org/10.1007/978-3-030-11726-9_6.
- Moucheng Xu, Yukun Zhou, Chen Jin, Marius de Groot, Daniel C. Alexander, Neil P. Oxtoby, Yipeng Hu, and Joseph Jacob. Expectation maximisation pseudo labels. *Medical Image Analysis*, 94:103125, May 2024. ISSN 1361-8415. URL <http://dx.doi.org/10.1016/j.media.2024.103125>.
- Jingzhao Zhang, Tianxing He, Suvrit Sra, and Ali Jababai. Why gradient clipping accelerates training: A theoretical justification for adaptivity, 2020. URL <https://arxiv.org/abs/1905.11881>.

Appendix A. Further segmentation metrics

Table 11: Mean results on ATLAS hold-out set (N=131). Best score shown in bold. FPR values are shown as a multiple of 10^{-3} .

Modality	Model	Dice	HD95	AVD	ALD	LF1	TPR	FPR
T1w	Baseline	0.500	44.3	7.60	3.48	0.480	0.510	0.251
	Baseline+TTA	0.503	41.4	7.34	2.52	0.537	0.502	0.234
	Synth	0.456	47.4	8.73	2.26	0.536	0.426	0.200
	Synth+TTA	0.455	48.3	8.51	1.76	0.559	0.424	0.191

Table 12: Mean results on the ISLES2015 dataset (N=28). Best score per column is shown in bold. FPR values are shown as a multiple of 1000.

Modality	Model	Dice	HD95	AVD	ALD	LF1	TPR	FPR
T1w	Baseline	0.115	84.2	38.14	3.32	0.269	0.076	0.034
	Baseline+TTA	0.091	113.2	40.11	1.96	0.311	0.058	0.012
	Baseline+TENT	0.002	178.2	43.77	2.14	0.161	0.001	0.001
	Baseline+DAE	0.246	68.2	48.07	7.18	0.285	0.191	1.604
	Baseline+PL	0.040	81.6	42.79	643.29	0.003	0.039	1.979
	Baseline+UPL	0.000	256.0	43.79	2.11	0.000	0.000	0.000
	Baseline+DPL	0.000	256.0	43.79	2.11	0.000	0.000	0.000
	Synth	0.222	70.5	30.49	7.14	0.208	0.168	0.162
	Synth+TTA	0.230	78.5	31.41	2.18	0.349	0.163	0.085
	Synth+TENT	0.076	108.2	33.79	40.86	0.103	0.058	0.265
	Synth+DAE	0.268	58.1	29.18	3.64	0.316	0.223	0.293
	Synth+PL	0.050	76.9	42.55	3.93	0.321	0.028	0.008
	Synth+UPL	0.000	241.7	43.79	2.04	0.050	0.000	0.000
	Synth+DPL	0.001	221.7	43.77	2.46	0.127	0.000	0.000
T2w	Baseline	0.007	65.4	50.81	15.00	0.078	0.044	2.786
	Baseline+TTA	0.003	65.5	48.97	6.86	0.095	0.025	2.260
	Baseline+TENT	0.001	142.6	43.38	3.75	0.050	0.001	0.085
	Baseline+DAE	0.006	71.5	88.17	9.43	0.071	0.069	5.805
	Baseline+PL	0.002	74.2	71.28	155.21	0.013	0.005	5.055
	Baseline+UPL	0.000	256.0	43.79	2.11	0.000	0.000	0.000
	Baseline+DPL	0.000	256.0	43.79	2.11	0.000	0.000	0.000
	Synth	0.231	74.8	52.73	11.82	0.166	0.443	3.534
	Synth+TTA	0.245	74.6	50.99	4.68	0.279	0.454	3.379
	Synth+TENT	0.215	77.4	33.44	20.11	0.109	0.276	1.755
	Synth+DAE	0.255	63.1	31.10	4.61	0.280	0.328	1.437
	Synth+PL	0.245	73.3	37.57	13.71	0.161	0.288	2.280
	Synth+UPL	0.152	63.3	31.06	12.43	0.138	0.116	0.631
	Synth+DPL	0.111	58.6	35.25	8.11	0.172	0.073	0.143
FLAIR	Baseline	0.000	71.4	40.06	10.79	0.018	0.000	0.515
	Baseline+TTA	0.000	112.9	41.24	3.43	0.000	0.000	0.238
	Baseline+TENT	0.000	119.0	43.47	4.32	0.000	0.000	0.021
	Baseline+DAE	0.000	80.1	61.65	15.29	0.015	0.004	3.679
	Baseline+PL	0.000	77.1	43.43	70.43	0.009	0.000	0.490
	Baseline+UPL	0.000	256.0	43.79	2.11	0.000	0.000	0.000
	Baseline+DPL	0.000	256.0	43.79	2.11	0.000	0.000	0.000
	Synth	0.314	62.9	18.84	10.61	0.154	0.346	0.975
	Synth+TTA	0.329	82.1	18.37	3.50	0.275	0.359	0.891
	Synth+TENT	0.127	79.0	28.03	34.54	0.031	0.107	0.460
	Synth+DAE	0.274	55.7	20.25	7.86	0.152	0.305	0.989
	Synth+PL	0.252	75.7	50.59	111.43	0.036	0.330	3.176
	Synth+UPL	0.232	137.9	24.88	3.04	0.271	0.187	0.111
	Synth+DPL	0.205	145.6	25.16	7.36	0.236	0.168	0.191
DWI	Baseline	0.000	80.1	42.63	5.54	0.023	0.000	0.138
	Baseline+TTA	0.000	102.8	43.83	2.43	0.000	0.000	0.133
	Baseline+TENT	0.000	103.9	43.52	1.89	0.000	0.000	0.021
	Baseline+DAE	0.000	76.2	40.04	11.21	0.025	0.000	2.123
	Baseline+PL	0.004	77.5	40.33	835.36	0.001	0.004	0.726
	Baseline+UPL	0.000	256.0	43.79	2.11	0.000	0.000	0.000
	Baseline+DPL	0.000	256.0	43.79	2.11	0.000	0.000	0.000
	Synth	0.193	82.5	47.64	16.71	0.100	0.352	2.741
	Synth+TTA	0.204	81.1	44.32	8.39	0.187	0.336	2.344
	Synth+TENT	0.104	86.6	30.71	38.50	0.051	0.108	0.882
	Synth+DAE	0.185	80.4	39.10	12.36	0.106	0.262	2.139
	Synth+PL	0.186	85.2	81.64	17.43	0.120	0.397	5.759
	Synth+UPL	0.179	60.8	32.42	19.43	0.154	0.155	0.268
	Synth+DPL	0.089	117.4	39.27	3.75	0.300	0.060	0.031
Ensemble	Baseline	0.000	242.8	43.79	2.00	0.000	0.000	0.000
	Baseline+TTA	0.000	256.0	43.79	2.11	0.000	0.000	0.000
	Baseline+TENT	0.000	256.0	43.79	2.11	0.000	0.000	0.000
	Baseline+DAE	0.000	231.0	43.68	2.00	0.000	0.000	0.007
	Baseline+PL	0.000	198.9	43.79	2.11	0.024	0.000	0.000
	Baseline+UPL	0.000	256.0	43.79	2.11	0.000	0.000	0.000
	Baseline+DPL	0.000	256.0	43.79	2.11	0.000	0.000	0.000
	Synth	0.370	60.4	19.68	7.50	0.234	0.339	0.256
	Synth+TTA	0.378	69.7	20.01	2.75	0.348	0.334	0.223
	Synth+TENT	0.111	114.8	32.23	3.21	0.235	0.089	0.047
	Synth+DAE	0.365	51.4	19.84	3.75	0.354	0.331	0.204
	Synth+PL	0.246	60.7	29.01	21.18	0.125	0.188	0.150
	Synth+UPL	0.016	218.2	42.52	5.18	0.131	0.009	0.000
	Synth+DPL	0.033	187.3	41.09	6.04	0.223	0.020	0.000

Table 13: Mean results on the ARC dataset (N=229). Best score per column is shown in bold. FPR values are shown as a multiple of 1000.

Modality	Model	Dice	HD95	AVD	ALD	LF1	TPR	FPR
T1w	Baseline	0.646	24.5	18.04	6.19	0.335	0.600	1.178
	Baseline+TTA	0.648	23.7	18.33	3.42	0.442	0.598	1.126
	Baseline+TENT	0.077	144.9	75.50	3.51	0.180	0.060	0.285
	Baseline+DAE	0.614	26.2	26.53	3.15	0.507	0.685	2.238
	Baseline+PL	0.325	67.5	146.72	175.61	0.017	0.613	10.342
	Baseline+UPL	0.341	74.4	48.10	22.84	0.244	0.262	0.695
	Baseline+DPL	0.340	52.5	52.48	9.53	0.324	0.247	0.465
	Synth	0.609	27.9	22.88	1.99	0.613	0.539	0.953
	Synth+TTA	0.611	27.0	24.08	1.84	0.640	0.534	0.885
	Synth+TENT	0.560	33.4	26.71	2.42	0.528	0.604	2.385
	Synth+DAE	0.613	23.4	20.60	2.26	0.581	0.640	1.903
	Synth+PL	0.311	158.6	48.41	260.54	0.017	0.310	2.303
	Synth+UPL	0.340	56.3	54.57	20.35	0.334	0.243	0.457
	Synth+DPL	0.255	58.3	63.36	7.44	0.530	0.169	0.339
T2w	Baseline	0.040	76.8	73.80	47.12	0.044	0.063	6.778
	Baseline+TTA	0.023	77.0	71.83	26.00	0.054	0.036	6.819
	Baseline+TENT	0.000	148.5	85.40	5.11	0.047	0.000	0.206
	Baseline+DAE	0.056	75.8	123.49	10.09	0.113	0.134	10.938
	Baseline+PL	0.006	78.8	127.78	353.31	0.007	0.014	12.731
	Baseline+UPL	0.000	256.0	85.74	2.57	0.013	0.000	0.185
	Baseline+DPL	0.000	256.0	85.74	2.57	0.013	0.000	0.185
	Synth	0.299	66.2	40.79	38.81	0.060	0.304	2.282
	Synth+TTA	0.284	66.2	43.70	16.00	0.117	0.274	1.893
	Synth+TENT	0.321	55.5	43.43	15.09	0.140	0.326	1.663
	Synth+DAE	0.437	40.8	40.19	11.43	0.196	0.410	1.344
	Synth+PL	0.384	65.5	40.26	22.77	0.095	0.475	3.881
	Synth+UPL	0.120	50.7	73.30	22.71	0.172	0.074	0.484
	Synth+DPL	0.055	52.3	78.43	47.28	0.108	0.032	0.447
FLAIR	Baseline	0.193	66.2	52.15	49.49	0.049	0.205	4.532
	Baseline+TTA	0.202	65.7	47.98	25.98	0.090	0.197	3.719
	Baseline+TENT	0.011	165.6	79.40	4.94	0.070	0.008	0.628
	Baseline+DAE	0.287	54.8	75.47	11.09	0.232	0.327	5.981
	Baseline+PL	0.126	81.9	162.13	382.66	0.007	0.240	13.548
	Baseline+UPL	0.000	256.0	82.36	2.62	0.035	0.000	0.497
	Baseline+DPL	0.000	256.0	82.36	2.62	0.035	0.000	0.497
	Synth	0.199	59.3	60.36	17.69	0.150	0.157	1.349
	Synth+TTA	0.190	56.4	62.98	8.36	0.256	0.143	1.185
	Synth+TENT	0.340	49.7	46.05	5.01	0.247	0.286	1.582
	Synth+DAE	0.263	51.5	53.14	5.88	0.248	0.215	1.581
	Synth+PL	0.276	96.8	45.97	93.18	0.027	0.255	2.133
	Synth+UPL	0.029	99.1	80.44	4.79	0.272	0.016	0.520
	Synth+DPL	0.010	146.9	81.38	7.11	0.189	0.005	0.512
Ensemble	Baseline	0.107	53.3	77.04	22.20	0.309	0.071	1.137
	Baseline+TTA	0.087	65.8	78.91	9.10	0.429	0.057	1.126
	Baseline+TENT	0.003	238.0	85.73	2.60	0.054	0.002	0.185
	Baseline+DAE	0.212	51.3	73.84	39.25	0.168	0.212	2.350
	Baseline+PL	0.016	76.1	70.76	512.92	0.004	0.014	3.869
	Baseline+UPL	0.000	256.0	85.74	2.57	0.013	0.000	0.185
	Baseline+DPL	0.000	256.0	85.74	2.57</			